Additive Manufacturing 41 (2021) 101956

Contents lists available at ScienceDirect

Additive Manufacturing

journal homepage: www.elsevier.com/locate/addma

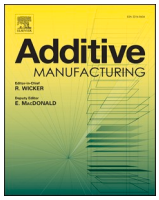

Thermal modeling in metal additive manufacturing using graph theory – Application to laser powder bed fusion of a large volume impeller

Reza Yavari [a], Richard Williams [b], Alex Riensche [a], Paul A. Hooper [b], Kevin D. Cole [a], Lars Jacquemetton [c], Harold (Scott) Halliday [d], Prahalada Krishna Rao [a,*]

[a] Mechanical and Materials Engineering, University of Nebraska-Lincoln, Lincoln, NE, USA
[b] Department of Mechanical Engineering, Imperial College, London, UK
[c] Sigma Labs, Santa Fe, NM, USA
[d] Center for Advanced Manufacturing, Navajo Technical University, Crownpoint, NM, USA

ARTICLE INFO

Keywords:
Metal additive manufacturing
Thermal history
Mesh-free simulation
Graph theory
Large volume parts

ABSTRACT

Despite its potential to overcome the design and processing barriers of traditional subtractive and formative manufacturing techniques, the use of laser powder bed fusion (LPBF) metal additive manufacturing is currently limited due to its tendency to create flaws. A multitude of LPBF-related flaws, such as part-level deformation, cracking, and porosity are linked to the spatiotemporal temperature distribution in the part during the process. The temperature distribution, also called the thermal history, is a function of several factors encompassing material properties, part geometry and orientation, processing parameters, placement of supports, among others. These broad range of factors are difficult and expensive to optimize through empirical testing alone. Consequently, fast and accurate models to predict the thermal history are valuable for mitigating flaw formation in LPBF-processed parts. In our prior works, we developed a graph theory-based approach for predicting the temperature distribution in LPBF parts. This mesh-free approach was compared with both non-proprietary and commercial finite element packages, and the thermal history predictions were experimentally validated with in-situ infrared thermal imaging data. It was found that the graph theory-derived thermal history predictions converged within 30–50% of the time of non-proprietary finite element analysis for a similar level of prediction error. However, these prior efforts were based on small prismatic and cylinder-shaped LPBF parts. In this paper, our objective was to scale the graph theory approach to predict the thermal history of large volume, complex geometry LPBF parts. To realize this objective, we developed and applied three computational strategies to predict the thermal history of a stainless steel (SAE 316L) impeller having outside diameter 155 mm and vertical height 35 mm (700 layers). The impeller was processed on a Renishaw AM250 LPBF system and required 16 h to complete. During the process, in-situ layer-by-layer steady state surface temperature measurements for the impeller were obtained using a calibrated longwave infrared thermal camera. As an example of the outcome, on implementing one of the three strategies reported in this work, which did not reduce or simplify the part geometry, the thermal history of the impeller was predicted with approximate mean absolute error of 6% (standard deviation 0.8%) and root mean square error 23 K (standard deviation 3.7 K). Moreover, the thermal history was simulated within 40 min using desktop computing, which is considerably less than the 16 h required to build the impeller part. Furthermore, the graph theory thermal history predictions were compared with a proprietary LPBF thermal modeling software and non-proprietary finite element simulation. For a similar level of root mean square error (28 K), the graph theory approach converged in 17 min, vs. 4.5 h for non-proprietary finite element analysis.

* Corresponding author.
E-mail address: rao@unl.edu (P.K. Rao).

https://doi.org/10.1016/j.addma.2021.101956
Received 12 October 2020; Received in revised form 13 January 2021; Accepted 9 March 2021
Available online 19 March 2021

1. Introduction

1.1. Motivation

In the laser powder bed fusion (LPBF) process thin layers of powder material are raked or rolled on a platen (powder bed) and selectively melted layer-upon-layer using a laser to form a three-dimensional part [1]. A key advantage of the LPBF process is that it can reduce multiple sub-components to a single part due to its ability to create complex features, such as conformal cooling channels, which are difficult, if not impossible, to achieve with traditional subtractive and formative processes [2]. The fewer number of parts leads to reduction in both weight and production costs [1]. For example, General Electric developed a turboprop engine that consolidated 855 separate parts into just twelve LPBF-processed parts, which reduced the weight of the engine by over 100 lb., and increased its power by 10% [3].

Despite these advantages, the LPBF process tends to create flaws, such as porosity and deformation in geometry, which in turn can lead to inconsistencies in the functional properties of the final part [4]. The large variation in part quality hinders the adoption of LPBF in safety-critical applications, such as aerospace and biomedical industries.

Flaw formation in LPBF is influenced by the temperature distribution and cooling rate in the part as it is being built [5,6]. Depending on its shape, certain regions of the part may retain heat or cool more slowly compared to others. The uneven heating and cooling of the part is the root cause of flaw formation in LPBF, such as non-uniformity of microstructure, deformation and cracking [7]. This spatiotemporal temperature distribution, often called the thermal history, is a complex function of the part shape (design), processing parameters, build plan (layout), and material properties [8]. Therefore, parameters optimized by empirical testing of simple-shaped coupons followed by data-driven process monitoring may not work for all part shapes [9,10].

The consequential effect of part design on the temperature distribution, and ultimately on part quality is exemplified in Fig. 1, which shows a stainless steel knee implant built on a commercial-grade LPBF machine. The knee implant has an overhang region, i.e., a part feature where the underside is devoid of material and thus requires anchoring supports to prevent collapse. Although the knee implant was processed under manufacturer-recommended settings, the poor thermal conductivity of the un-melted powder underneath the overhang section and the narrow cross-section of the supports impede heat flow. The heat constrained in the overhang region, in turn, led to microstructure heterogeneity and degraded surface quality [11–13].

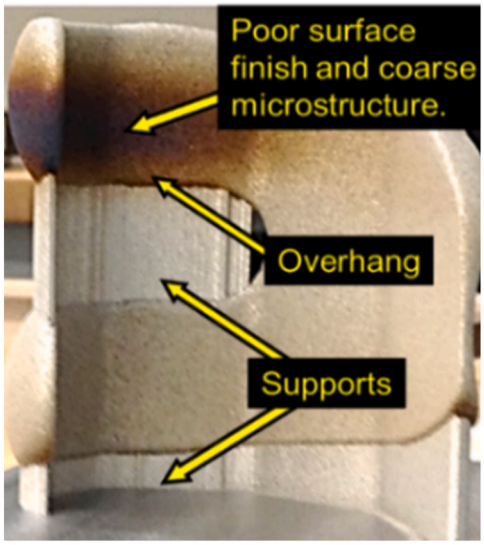

Fig. 1. A ~70 mm tall LPBF knee implant with a steep overhang feature shows poor surface finish, and coarse microstructure.

For ensuring part quality, AM practitioners currently employ expensive, multi-stage empirical tests to optimizi processing parameters, finalize the part design, suggest the location and orientation of parts on the build plate, and ascertain placement of anchoring supports [9]. For example, the effect of parameters, such as the laser power and velocity on microstructure and porosity have been quantified in the literature [14–16]. These optimal parameter sets were developed in the context of single-track scans, and simple shapes – typically prismatic coupons and so-called dogbone geometries – due to their tractability for post-process materials characterization and mechanical testing [7,17]. However, prior research has showed that process parameters optimized for one type of geometry may not lead to a flaw-free part when used for different part geometries and orientations [6,18].

Resorting to a purely empirical optimization approach is prohibitively expensive and time consuming in LPBF given the cost of the powder, relative slow speed of the process, and limited number of samples available for testing [19]. Accordingly, fast and accurate models to predict the temperature distribution in LPBF parts are valuable in the following contexts [8,20–22].

- Reduce empirical testing needed for optimization of processing parameters, part features, placement of supports, and build conditions.
- Augment in-situ sensor data for process monitoring and control.
- Predict residual stresses, microstructure evolved, and mechanical properties.

Despite the extensive research in computational thermal modeling in LPBF using finite element analysis, two challenges are identified in the literature [23,24]: (1) predicting the temperature distribution in large volume, complex-shaped LPBF parts, and (2) validating the model predictions with in-situ measurements [20]. These gaps are discussed in depth in Section 2.

Existing commercial packages such as Netfabb and Ansys Additive predominantly use finite element (FE) analysis to predict the temperature distribution [23,25]. While these commercial packages can predict the temperature distribution well within the time to build the part, however, the implementation and physical approximations incorporated within these commercial software packages remain proprietary, and the accuracy of their predictions remain to be independently validated [20,26].

Although non-proprietary FE-based thermal models of the LPBF process have been published and validated in the literature, a major gap in these efforts is that the thermal history predictions are made in the context of simple prismatic shapes with low thermal mass [20,26]. A second drawback is that the non-proprietary simulations often require longer to converge than the actual time to build the part, chiefly due to bottlenecks concerned with FE-mesh generation [25]. Therefore, a burgeoning need is to develop computationally efficient thermal models to predict the temperature distribution in large volume, complex shaped LPBF parts, and subsequently, quantify the prediction accuracy with in-situ measurements. This paper is focussed on addressing the foregoing research need.

1.2. Objective

In our previous papers, we developed and validated a mesh-free, graph theory-based approach for predicting the temperature distribution (thermal history) of LPBF parts [27–29]. In these prior works we compared the graph theory approach to FE analysis and reported that the graph theory predictions converged within 30–50% of the time required for non-proprietary FE analysis for a similar level of prediction error [27–29]. However, a gap in our prior work is that the graph theory approach was tested with simple prismatic, cylindrical, and cone-shaped geometries.

The objective of this paper is to scale the graph theory approach to

predict the thermal history of large-volume and complex-shaped LPBF parts. To realize this objective, three computational strategies to scale the graph theory approach were developed and tested. The test part used in this work (Fig. 2) was a stainless steel (SAE 316L) impeller. This part was processed on a commercial LPBF system (Renishaw AM250). The impeller had an outside diameter approximately 155 mm, vertical height 35 mm (250 cm^3 volume), and consisted of 700 layers (50 μm layer thickness). The impeller in Fig. 2 had a spiraling internal channel, and 15 thin-walled fin-like structures each of 4 mm width. The build time was close to 16 h. The steady state surface temperature for each layer of the impeller was recorded using an in-situ thermal camera. The steady state surface temperature is obtained after a layer of powder is deposited. In effect, the steady state surface temperature is the end-of-cycle temperature after a fresh layer is deposited, but before it is melted by the laser.

Using one of the computational approaches developed in this work, the thermal history of the impeller was simulated within 40 min compared to 16 h build time while maintaining the prediction error ~6% (mean absolute percentage error) and within 25 K (root mean squared error) of the experimental data. The standard deviation is 0.8% and 3.7 K respectively. The part geometry was not scaled to make it simpler or smaller, and the simulations were conducted on a desktop computer in the Matlab environment.

1.3. Challenges with FE-based thermal modeling in AM and prior work in graph theory

The main reason for the computational efficiency of the graph theory approach over FE analysis is explained in Section 3.3.3; we provide a brief explanation herewith. To obtain the thermal history it is necessary to solve the heat diffusion equation. Solving the heat diffusion equation is challenging problem in the additive manufacturing context, including LPBF, because, the shape of the part (object) is not static but changes as material is continually added layer-upon-layer [20]. Consequently, for thermal simulation concerning any metal additive manufacturing process the part geometry must be repeatedly re-meshed. In other words, the computational domain of FE-based models in AM changes after each time step. The re-meshing interval can range from the individual hatch-level to deposition of multiple layers at once depending upon the desired resolution. This remeshing is a computationally demanding and time-consuming step as it is necessary to label and track the location of each FE node. Researchers use two popular approaches to simulate the deposition of material in FE analysis, namely, element birth-and-death method and quiet element method [23,30]. A hybrid method is also used in some commercial software [23].

To further speed computation, these meshing strategies are combined with a dynamic technique called adaptive meshing [31,32]. In adaptive meshing, the element size is not fixed and changes continually during the simulation [33,34]. As the simulation progresses layer-by-layer, the element size is made larger (i.e., the mesh is made coarse) for regions of the part that have a large, bulkier cross-section, whereas regions near the boundary of the part and those with intricate features tend to have a finer mesh. To speed computation, commercial packages have devised proprietary techniques to implement adaptive meshing [33–39].

Next, in FE methods the continuum heat diffusion equation must be solved for each element, which requires matrix inversion, placing further computational demands. The graph theory approach has three computational advantages over FE analysis. First, the graph theory approach is mesh-free. Second, it solves a discrete version of the heat diffusion equation that replaces matrix inversion with the matrix transpose. Third, the heat diffusion equation is solved without stepping through time [27–29].

We briefly review our prior work in predicting the temperature distribution in LPBF using graph theory [27–29]. Previously, in Ref. [28], we verified the graph theory approach with an FE-based implementation of Goldak's double ellipsoid thermal model, and qualitatively compared the graph theory-derived predictions with a commercial package (Netfabb by Autodesk) [40].

In Ref. [29] the precision of the temperature trends predicted by

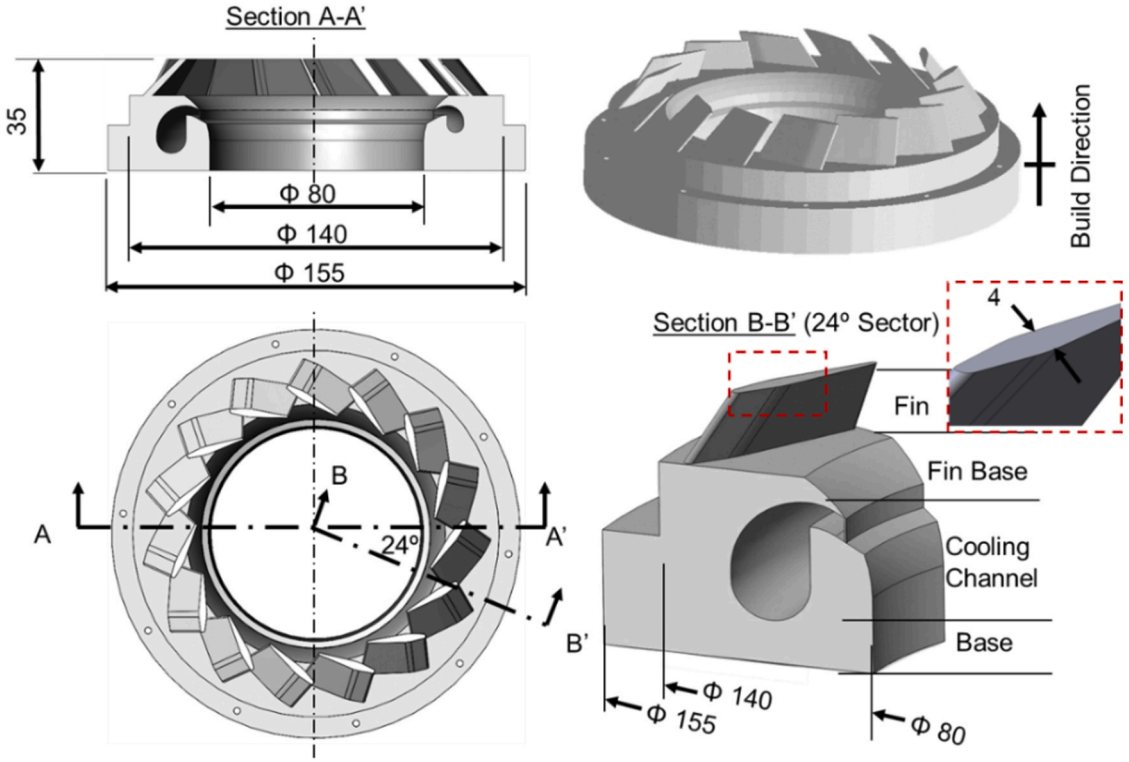

Fig. 2. Schematic of the impeller-shaped geometry studied in this work (all dimensions are in mm).

graph theory approach was verified with Green's function-based exact analytical solutions, finite element and finite difference methods for a variety of one- and three-dimensional benchmark heat transfer problems.

In Ref. [27] we experimentally validated the graph theory approach with surface temperature measurements obtained using an in-situ longwave infrared thermal camera for two LPBF parts, specifically, a cylinder (Φ 10 mm × 60 mm vertical height) and a cone-shaped part (Φ 10 mm × 20 mm vertical height). Additionally, in Ref. [27] both the graph theory and finite element-derived thermal history predictions were compared with experimental temperature measurements. As an example, for the cylinder-shaped test part, the graph theory approach predicted the surface temperature trends to within 10% mean absolute percentage error and 16 K root mean squared error compared to experimental measurements. Furthermore, the graph theory-based temperature predictions were made in less than 65 min, which was substantially faster than the actual time of 171 min required to build the cylinder. In comparison, for an identical level of resolution and prediction error, the non-proprietary FE-based approach required over 175 min

The rest of this paper is structured as follows. In Section 2, we summarize the challenges in thermal modeling and validation in LPBF. In Section 3, we describe the experimental methodology, provide a brief background of the graph theory approach, and detail the three computational strategies for scaling the graph theory. Results from implementing the graph theory approach to the impeller part, along with comparison with non-proprietary FE analysis, and Netfabb are reported Section 4. Lastly, the conclusions are summarized in Section 5.

2. Literature review

The complex thermal interactions specific to LPBF process are depicted in Fig. 3. The thermal phenomena in LPBF encompass conductive, convective and radiative heat transfer, across three scales, namely, meltpool (~100 μm), powder bed (< 1 mm), and part-level (> 1 mm) [30,41].

This work relates to the part-level thermal aspects which are in turn are influenced by the material properties, part design, build plan, and processing parameters, such as laser power and velocity settings [42,43]. We summarize the recent research and challenges in the prediction and subsequent experimental validation of the part temperature distribution for large volume components.

2.1. Part-scale thermal modeling in LPBF

Thermal modeling is the first in a chain of requirements in the metal additive manufacturing industry. A key need is to extend thermal modeling for predicting microstructure, residual stresses (deformation), and mechanical properties of LPBF parts [20,44,45]. This is a significant challenge as the length-scale for the causal thermal phenomena range from sub-micrometer (microstructure-level) to tens of millimeters (part-level). Hence inaccuracies in the prediction of the temperature distribution will be magnified when used in other models.

Apart from accuracy, to be practically useful, thermal models must be computationally efficient when scaled to practical-scale parts with complex geometry. An important measure of computational efficiency is the simulation time, which must ideally be less than the time required to print the part. In this context, a majority of thermal modeling efforts have focused on prismatic geometries at the part-level with typical build height of 25 mm, and single-track and one-layer test coupons at the microstructure and powder bed-levels, respectively [20,46]. Studies that reveal the fundamental relationship between the thermal distribution and the build quality for challenging shapes, such as thin sections, internal channels, and overhangs, placement of supports are being actively researched [11,13].

Existing commercial thermal simulation packages in AM predominantly use the FE method [20,23]. As explained previously, a main challenge in FE-based modeling of the LPBF process is that the shape of the part continually changes as material is deposited, and therefore the part has to be repeatedly re-meshed. The meshing of the part is the most time-consuming aspect of thermal modeling in AM. Moreover, the computation time for meshing scales exponentially with the volume of the part.

Besides proprietary meshing algorithms and opaque physical approximations, commercial packages do not allow the export of node-level temperature data needed for independent validation of the thermal distribution [33,47]. Furthermore, because in adaptive meshing the node size is not constant but changes layer-to-layer, there is likely to be an uncertainty in the temperature distribution predicted by commercial software for a given region. This uncertainty in temperature prediction is liable to cascade into other aspects, such as predicting the thermal-induced deformation of LPBF parts. Lastly, while commercial software packages have succeeded in reducing the computation time, researchers have identified the bourgeoning need for rigorous quantification of the uncertainty in thermal distribution and residual stress predictions introduced by adaptive meshing and physical approximations implemented therein [7].

Peter et al. [26] recently benchmarked five proprietary simulation software, namely, Atlas 3D Sunata, Additive Works Amphyon, MSC Simufact, Autodesk Netfabb, and Ansys Additive Print. The accuracy of these software was assessed with 11 different test geometries in terms of distortion prediction, distortion compensation, recoater crash, and support placement. The benchmarking study revealed a large variation in prediction accuracy between these commercial software, in one

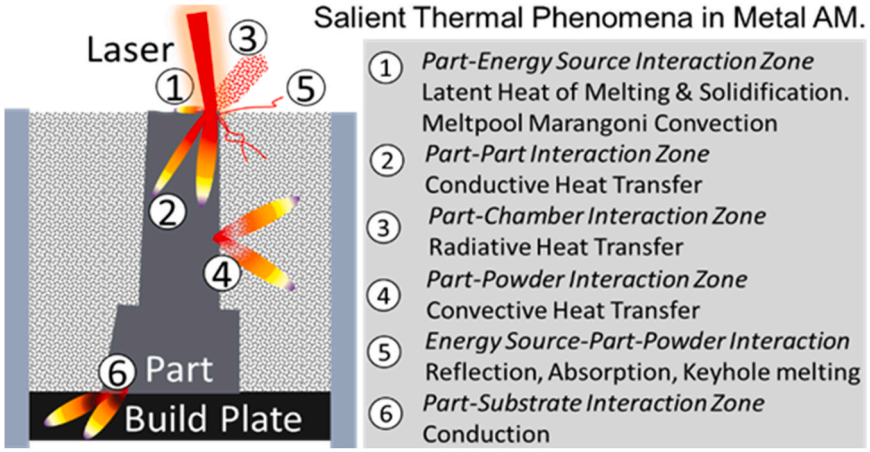

Fig. 3. The complex thermal phenomena in LPBF encompass conductive, convective, and radiative heat transfer at multiple scales.

instance the root mean square distortion prediction varied as much as 80%. Peter et al. note that each software had advantages and drawbacks, with respect to their predictive capabilities, and therefore a one-size-fits-all solution may therefore be elusive.

While non-proprietary FE models have been validated, the computation time is excessive, it takes days, if not hours to simulate the temperature distribution for a few layers [20,41]. As an example, Kundakcioglu et al. report that using FE-based thermal model to simulate just 1 min of LPBF processing for a dia. 2 mm × 0.3 mm impeller required 20 h of desktop computing [48]. To overcome this impediment, researchers are actively developing mesh-free approaches to predict the effect of thermal history on part quality. For example, Hoelzle and co-workers, developed a thermal modeling approach based on the analogy of an electrical network to reduce the computation burden [49].

Recently, To and co-workers introduced a GPU-based thermal modeling approach, and tested their approach with non-proprietary adaptive meshing FE techniques and experimental LPBF data [50]. The test part included a cube of side 20 mm, and the temperature during the build was measured using a K-type thermocouple embedded in the center of the build plate. Their simulation approach when combined with adaptive meshing strategies showed over 4–5-fold improvement in the computation time over conventional FE-based approaches.

2.2. Measurement and validation of thermal trends in LPBF

In the context of validation of thermal models in LPBF, research has been predominantly focused on predicting the temperature distribution for few layers of simple prismatic and cylindrical shapes using contact-based thermocouples [36,51,52]. The temperature distribution is subsequently correlated with microstructure evolved and distortion due to residual stress [26,32,46,53].

Temperature measurements in the literature were made using contact thermocouples embedded in the build plate or touching the bottom of the part [36,51,52]. A key drawback is that thermocouples embedded in the build plate or brazed to the bottom of the part could only track the temperature for that specific point, and not the entire part volume or surface. Further, a thermocouple embedded within the bottom of the part or the build plate would not sufficiently capture the temperature distribution on the top surface as the layers are progressively deposited and the part grows in size. While it is conceivable to embed thermocouples within the part after stopping the process, this approach is time-consuming, and would inherently alter the thermal history and build conditions.

Promoppatum et al. [54]. studied the effect temperature distribution in a large LPBF-processed Inconel 718 test part measuring about 200 mm × 100 mm × 60 mm (build height) and consisting of 1200 layers. During the build, temperature data for five points at the bottom of the test part were acquired with thermocouples embedded within the build plate, such that the head of thermocouple is exposed. The temperature readings acquired by the thermocouple plateaued to 200 °C within 25 layers. Similar plateauing of the temperature trends as a function of the build height has been observed in the work of To and co-workers [50].

An alternative approach to using thermocouples, is to measure the surface temperature of the part using an infrared thermal camera, as demonstrated in our recent publications [6,27]. The concern with use of thermal imaging is that the surface temperature recorded by the thermal camera is not the absolute temperature but a relative trend. This is because the temperature measured by the thermal camera depends on the moment-by-moment emissivity of the surface observed. The emissivity is not constant but is a function of the temperature of the measured surface, its roughness, and inclination of the thermal camera to the surface [55].

In other words, the thermal camera must be calibrated to account for the emissivity of the part surface. Hyperspectral thermal imaging and two-wavelength pyrometry are alternative approaches to obtaining the temperature distribution without adjusting for emissivity [55–57]. The approach used to calibrate the thermal camera accounting for the material emissivity is described in depth in Section 3.2.1.

3. Methods

3.1. Experiments

The stainless steel (SAE 316L) impeller shown in Fig. 2 was processed on a Renishaw AM 250 LPBF system with the build plate pre-heated to about 450 K (180 °C). The build parameters are reported in Table 1. The experimental setup, shown in Fig. 4, included an infrared thermal camera (FLIR A35X) with wavelength in the 7–13 μm range (i.e., the longwave infrared spectrum). This setup is identical to the one used in our recent work [6,27].

The thermal camera was inclined at an angle of 66° to the horizontal and sealed inside a vacuum-tight box with a germanium window. Surface temperature data was acquired at the sampling rate of 60 Hz. The response time is approximately 12 ms. Thermal images were captured at 320 × 256 pixels with a resolution of approximately 1 mm^2 per pixel.

3.2. Data acquisition

3.2.1. Calibration of the thermal camera readings

The detailed calibration procedure for the thermal camera, including measurement uncertainty quantification, was described in two recent publications, Refs. [6,27]. Here we provide a brief summary. A thermocouple was inserted in a deep cavity of a LPBF-processed test artifact. The test artifact was subsequently heated in a controlled manner. The thermocouple in the cavity of the test artifact recorded the absolute temperature (of the test artifact), and its surface temperature was acquired with the thermal camera. Subsequently, the surface temperature trends measured by the thermal camera were mapped to the absolute temperature recorded by the thermocouple on fitting a calibration function.

The calibration process is repeated with powder spread over the test artifact, and a separate calibration function is developed. Calibration of the thermal camera with and without powder ensures that the temperature readings account for the change in material emissivity in LPBF after a layer of fresh powder is raked on top of a just-fused layer. To ascertain the measurement uncertainty in the thermal camera readings the calibration procedure is repeated ten times. The 95% confidence interval in temperature readings in the 300–800 K interval was in the range of 0.1–1% of the mean temperature reading [27].

Table 1
Summary of the material and processing parameters used for building the impeller.

Process Parameter	Values [units]
Laser type and wavelength.	200 W fiber laser, wavelength 1070 nm
Laser power, point distance, exposure time	200 W, 60 μm, 80 us
Inner border parameters - power, point distance, exposure time for the test part (center cylinder)	200 W, 40 μm, 90 us
Outer border parameters - power, point distance, exposure time (center cylinder)	110 W, 20 μm, 100 us
Hatch spacing	110 μm
Layer thickness	50 μm
Spot diameter of the laser	65 μm
Scanning strategy for the bulk section of the part	Meander-type scanning strategy with 45° rotation of scan path between layers.
Build atmosphere	Argon
Build plate preheat temperature	180 °C (~450 K)
Material type	SAE 316L stainless steel
Powder size distribution	10–45 μm

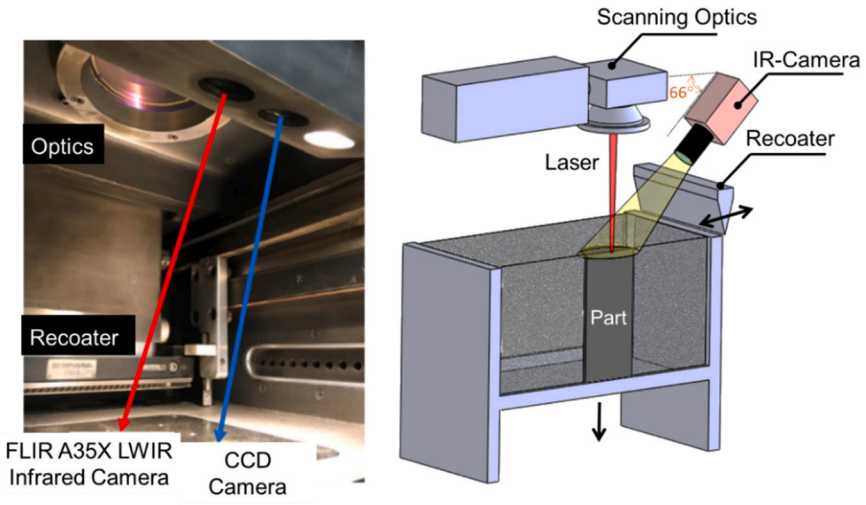

Fig. 4. The picture and schematic diagram of the experimental setup used in this work. A long wave infrared (LWIR) thermal camera was inclined at an angle of 66° to the horizontal.

3.2.2. Steady state surface temperature measurement

The region of the impeller from where the temperature data was sampled is shown in Fig. 5. This region was selected because it is the most contiguous solid volume cross-section within the part boundary in the vertical direction. Sampling near the boundary of the part was avoided owing to the limited spatial resolution of the thermal camera.

A 9-pixel × 9-pixel sample (9 mm × 9 mm area) in the main body of the part and a 2-pixel × 2-pixel sample (2 mm × 2 mm area) on the fin section were chosen for monitoring the surface temperature. The thin cross-section of the fin prevented sampling of a larger area. The top-view cross sections of the part for select layers and their corresponding infrared thermal images immediately after scanning the layers are shown alongside in Fig. 6.

The average raw surface temperature recorded for the regions sampled in Fig. 5 are tracked in Fig. 7(a) as function of the layer (build height). Shown in Fig. 7(b) is the raw surface temperature signature for a zoomed in portion that depicts the presence of three large spikes. The rationale for these temperature signatures is as follows.

(1) The large upward peak corresponds to the time when the laser was actively scanning the area demarcated in Fig. 5. The time elapsed between two upward spikes denotes the time between melting of successive layers, and is termed the interlayer cooling time (ILCT). The ILCT is effectively the time between layers.
(2) After the end of melting of a layer, the recoater returned to fetch fresh powder, and momentarily blocked the IR camera field-of-view resulting in a large downward spike.
(3) As the recoater deposited a fresh layer of powder, it again momentarily blocked the field-of-view of the IR camera, which caused a second downward spike in the temperature signal.
(4) Marked in Fig. 7(b) is the *steady state surface temperature* for each layer just before the laser starts scanning the next layer.

In Fig. 8(a), the steady state temperature is tracked as a function of the build height for the entire part. In Fig. 8(b) the ILCT is plotted as a function of the build height. Since the area to be scanned varies as a function of the build height, the ILCT changed continually throughout the build. For example, the annular base had a larger area, and hence it took longer to scan compared to the fin-shaped features near the top. As an example, the ILCT for the base was close to 105 s compared to 15 s for the fin. The smaller scan area and shorter ILCT of the fin-shaped features leads to accumulation of heat, which in turn will influence the microstructure evolved [58].

In Fig. 8(a), the temperature in the base region was initially low, as the heat was conducted away to the build plate and into the substrate owing to the large surface area of the base and relatively longer ILCT. The temperature increases as more layers are deposited because the surrounding powder acts as an insulating medium. The internal cooling channel tends to accumulate heat as the roof of the channel is unsupported (overhang), and there is unmelted powder trapped inside the cavity of the channel. The temperature increase is rapid in the fin region due to its small cross section, shorter ILCT, and overhanging geometry.

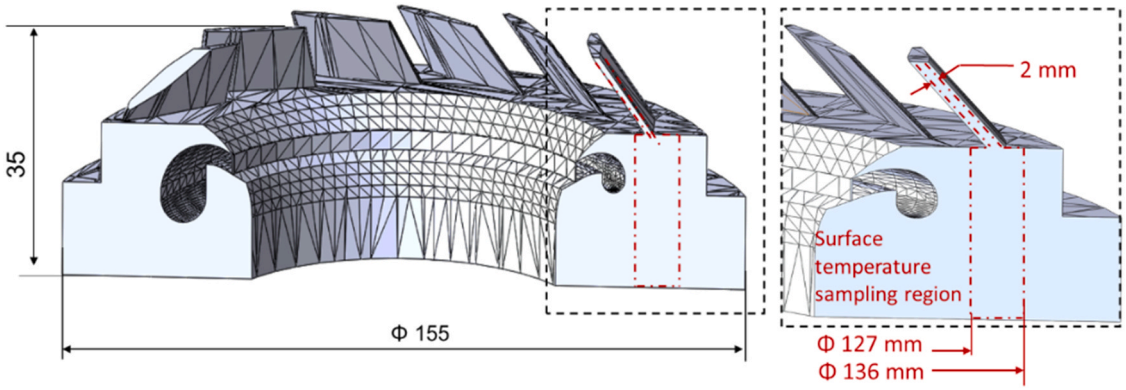

Fig. 5. Region where the surface temperature data is extracted for the impeller.

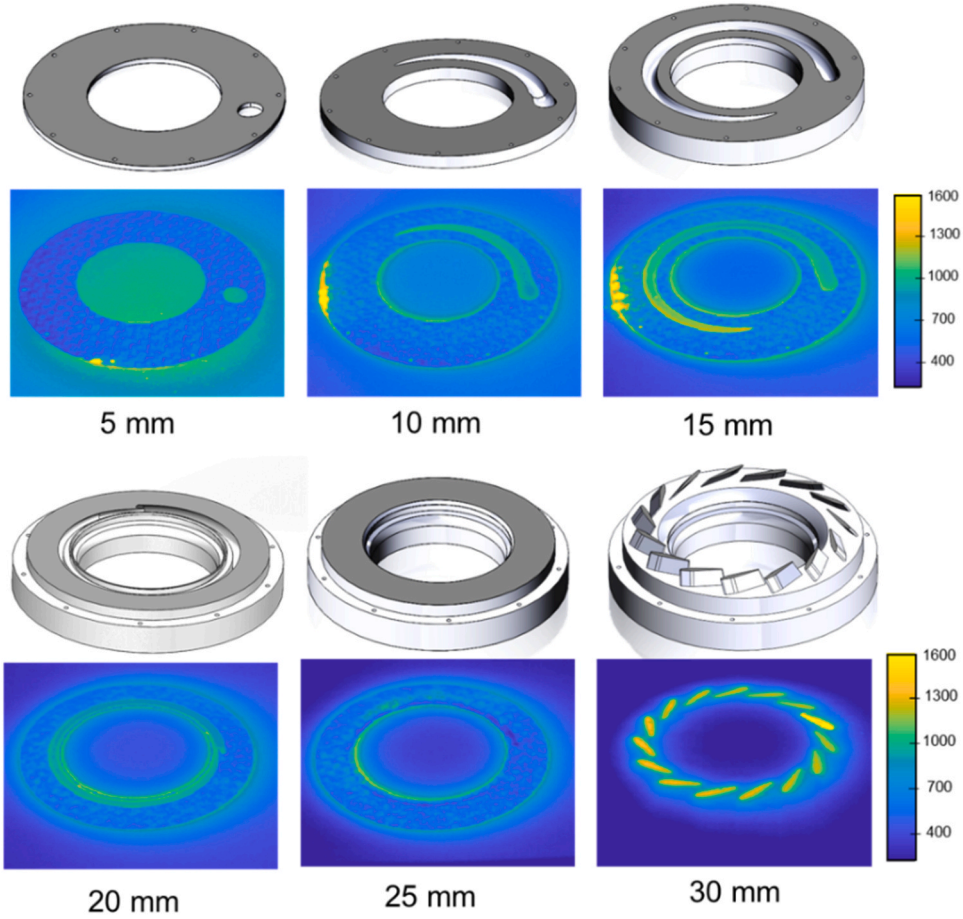

Fig. 6. CAD model and corresponding infrared thermal images of the part at different build heights immediately after the laser has finished melting the layer. The scale bar on the right is in Kelvin. The melting point of the material (SAE 316L) is 1600 K.

3.3. The graph theory approach for thermal modeling in LPBF

3.3.1. Solving the heat diffusion equation using graph theory

To predict the temperature distribution in a LPBF part it is necessary to solve the continuum heat diffusion equation, Eq. (1) [38]; FE analysis is chiefly used to solve the heat diffusion equation and obtain the thermal history of a part [22–25,38,41].

$$\overbrace{\rho c_p}^{Material\ Properties}\frac{\partial T(x,y,z,t)}{\partial t}-k\overbrace{\left(\frac{\partial^2}{\partial x^2}+\frac{\partial^2}{\partial y^2}+\frac{\partial^2}{\partial z^2}\right)}^{Shape\ of\ the\ Part}T(x,y,z,t)=\overbrace{\frac{P}{v\times h\times t}}^{Processing\ Parameters}=E_V \tag{1}$$

Solving the heat diffusion equation results in the temperature $T(x, y, z, t)$ for a location (x, y, z) inside a part at a time instant t. The term E_V on the right-hand side is called the energy density [J m^{-3}], and represents the energy supplied by the laser to melt a unit volume of material. The energy density E_V is a function of laser power (P [W]), distance between adjacent passes of the laser (h) [m], translation velocity (v) [m s^{-1}], and the layer thickness (t) [m]; these are the controllable parameters of the LPBF process.

The material properties are density ρ [kg m^{-3}], specific heat c_p [J kg^{-1} K^{-1}], and thermal conductivity k [W m^{-1} K^{-1}]. The effect of part shape is represented in the second derivative term on the left hand side of Eq. (1). The second derivative is called the *continuous Laplacian*. The graph theory approach solves a discrete form of the heat diffusion equation for the temperature. Then the temperature is adjusted to account for convective and radiative heat transfer phenomena (not shown in Eq. (1)). The following is the mathematical reasoning for the graph theory approach to solve the heat diffusion equation; this reasoning is discussed in detail in Ref. [29].

As in existing FE approaches, the energy density E_V in Eq. (1) is replaced by an initial temperature $T(x,y,z,\ t=0)=T_o$; where T_o is the melting point of the material.

$$\frac{\partial T(x,y,z,t)}{\partial\ \ t}-\alpha\left(\frac{\partial^2}{\partial x^2}+\frac{\partial^2}{\partial y^2}+\frac{\partial^2}{\partial z^2}\right)T(x,y,z,t)=0;\alpha=\frac{k}{\rho c_p} \tag{2}$$

Next, the heat diffusion equation is discretized over M nodes by substituting the second order derivative (continuous Laplacian) with the discrete Laplacian Matrix (L),

$$\frac{\partial T(x,y,z,t)}{\partial t}+\alpha(L)T(x,y,z,t)=0; \tag{3}$$

The eigenvectors (ϕ) and eigenvalues (Λ) of the Laplacian matrix (L) are found by solving the eigenvalue equation $L\phi=\phi\Lambda$. If the Laplacian matrix is constructed in a manner such that it is diagonally dominant and symmetric, its eigenvalues (Λ) will be non-negative, and the eigenvectors (ϕ) will form an orthogonal bases [59,60].

Because the transpose of an orthogonal matrix is the same as its inverse, hence, $\phi^{-1}=\phi'$ and $\phi\phi'=1$, then the eigenvalue equation $L\phi=\phi\Lambda$ may be post-multiplied by ϕ' to obtain $L=\ \ \phi\Lambda\phi'$.

Using this relationship in Eq. (3),

$$\frac{\partial T(x,y,z,t)}{\partial t}+\alpha(\phi\Lambda\phi')T(x,y,z,t)=0; \tag{4}$$

Eq. (4) is a first order, ordinary linear differential equation, which is easily solved as,

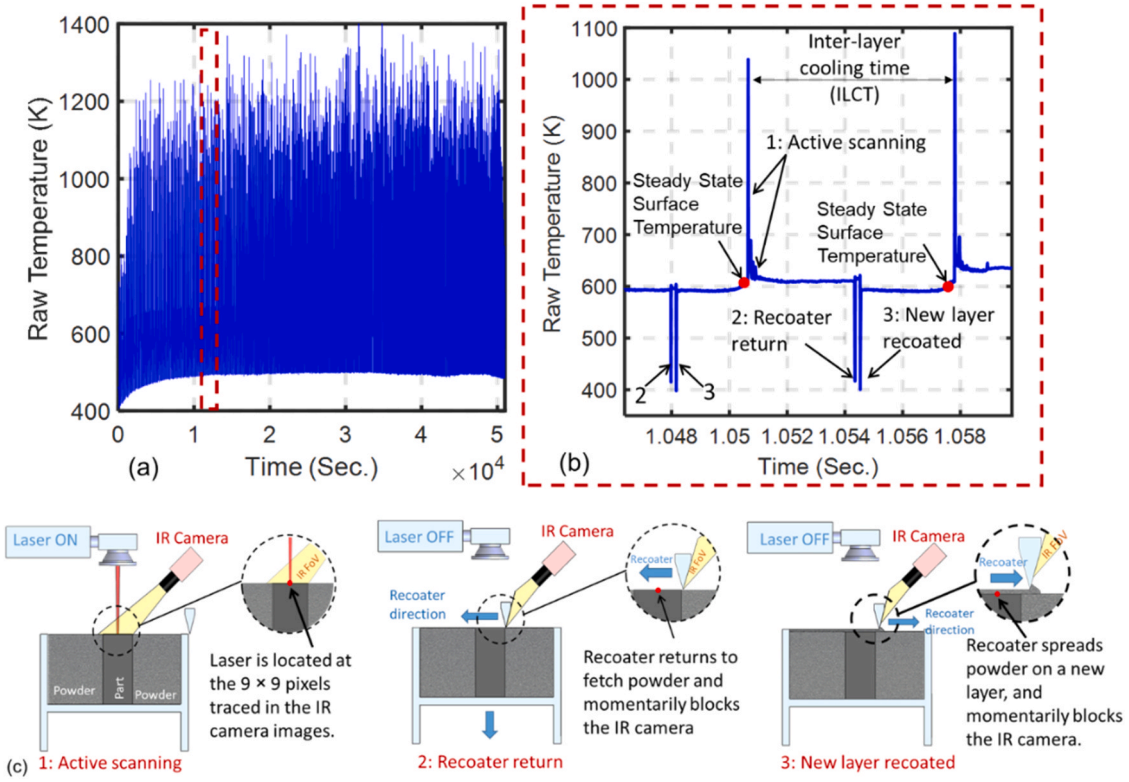

Fig. 7. (a) The raw surface temperature for the region sampled in Fig. 5. (b) zoomed in region from (a) showing the measurement of the steady state surface temperature just before the laser fuses a new layer. (c) The rationale for the various signatures observed in the raw temperature signature in (b).

$$T(x,y,z,t) = e^{-\alpha(\phi\Lambda\phi')t}T_o \tag{5}$$

The term $e^{-\alpha(\phi\Lambda\phi')t}$ is simplified via a Taylor series expansion,

$$e^{-\alpha(\phi\Lambda\phi')t} = 1 - \frac{\phi\Lambda\alpha t\phi'}{1!} + \frac{(\phi\Lambda\alpha t\phi')^2}{2!} - \frac{(\phi\Lambda\alpha t\phi')^3}{3!} + \dots$$

$$= 1 - \frac{\phi\Lambda\alpha t\phi'}{1!} + \frac{(\phi\Lambda\alpha t\phi')(\phi\Lambda\alpha t\phi')}{2!} - \frac{(\phi\Lambda\alpha t\phi')(\phi\Lambda\alpha t\phi')(\phi\Lambda\alpha t\phi')}{3!} + \dots$$

substituting $\phi\phi' = 1$,

$$e^{-\alpha(\phi\Lambda\phi')t} = \phi\phi' - \frac{\phi\Lambda\alpha t\phi'}{1!} + \frac{\phi(\Lambda\alpha t)^2\phi'}{2!} - \frac{\phi(\Lambda\alpha t)^3\phi'}{3!} + \dots = \phi e^{-\alpha\Lambda t}\phi' \tag{6}$$

Substituting, $e^{-\alpha(\phi\Lambda\phi')t} = \phi e^{-\alpha\Lambda t}\phi'$ into Eq. (5) gives,

$$T(x,y,z,t) = \phi e^{-\alpha\Lambda gt}\phi'\ T_o \tag{7}$$

Eq. (7) entails that the heat diffusion equation is solved as a function of the eigenvalues (Λ) and eigenvectors (ϕ) of the Laplacian Matrix (L), constructed on a discrete set of nodes. In Eq. (7) we introduced an adjustable coefficient g [m^{-2}] called the gain factor to calibrate the solution and adjust the units. The gain factor needs to be calibrated once for a particular material, and would thereafter remain constant.

Indeed, we used the same value of the gain factor from our previous works concerning the validation of the graph theory approach with thermography data obtained during LPBF of stainless steel parts [27].

3.3.2. Heat loss due to convection and radiation

Thus, per Eq. (7), the temperature of the nodes is estimated considering conductive heat transfer only. Next, heat loss due to radiation and convection at the top boundary of the part is included. For this purpose, we demarcate the nodes at the top boundary, and adjust the temperature of the boundary nodes (T_b) using lumped capacitive theory:

$$T_b = e^{-\tilde{h}(\Delta t)}\ (T_{bi} - T_\infty) + T_\infty \tag{8}$$

Where, T_∞ (= 300 K) is the temperature of the surroundings, T_{bi} is the initial temperature of the boundary nodes, T_b is the temperature of the boundary nodes after heat loss occurs, Δt is the dimensionless time between laser scans, and $\tilde{h}$ is the normalized combined coefficient of radiation (via Stefan-Boltzmann law) and convection (via Newton's law of cooling) from boundary to the surroundings [61].

3.3.3. Advantages and limiting assumptions of the graph theory approach

The graph theory approach has three inherent advantages over FE analysis.

(1) *Elimination of mesh-based analysis*. The graph theory approach represents the part as discrete nodes, which entirely eliminates the tedious meshing steps of FE analysis.
(2) *Elimination of matrix inversion steps*. While FE analysis rests on matrix inversion at each timestep for solving the heat diffusion equation, the graph theory approach is based on matrix multiplication operations, $T(x,y,z,t) = \phi e^{-\alpha\Lambda t}\phi'\ T_o$, which greatly reduces the computational burden.
(3) *Simplifying time stepping*. The time t for which the heat is diffused in the part in Eq. (7) can be set to one large time step without computing the temperature at intermediate discrete steps as in FE analysis.

To facilitate computation, the graph theory approach makes the following assumptions.

- *Heat transfer-related assumptions.* Material properties, such as the specific heat are considered to be constant, and do not change with temperature. Moreover, effect of the latent heat aspects is not considered. In other words, the effect change of state of material

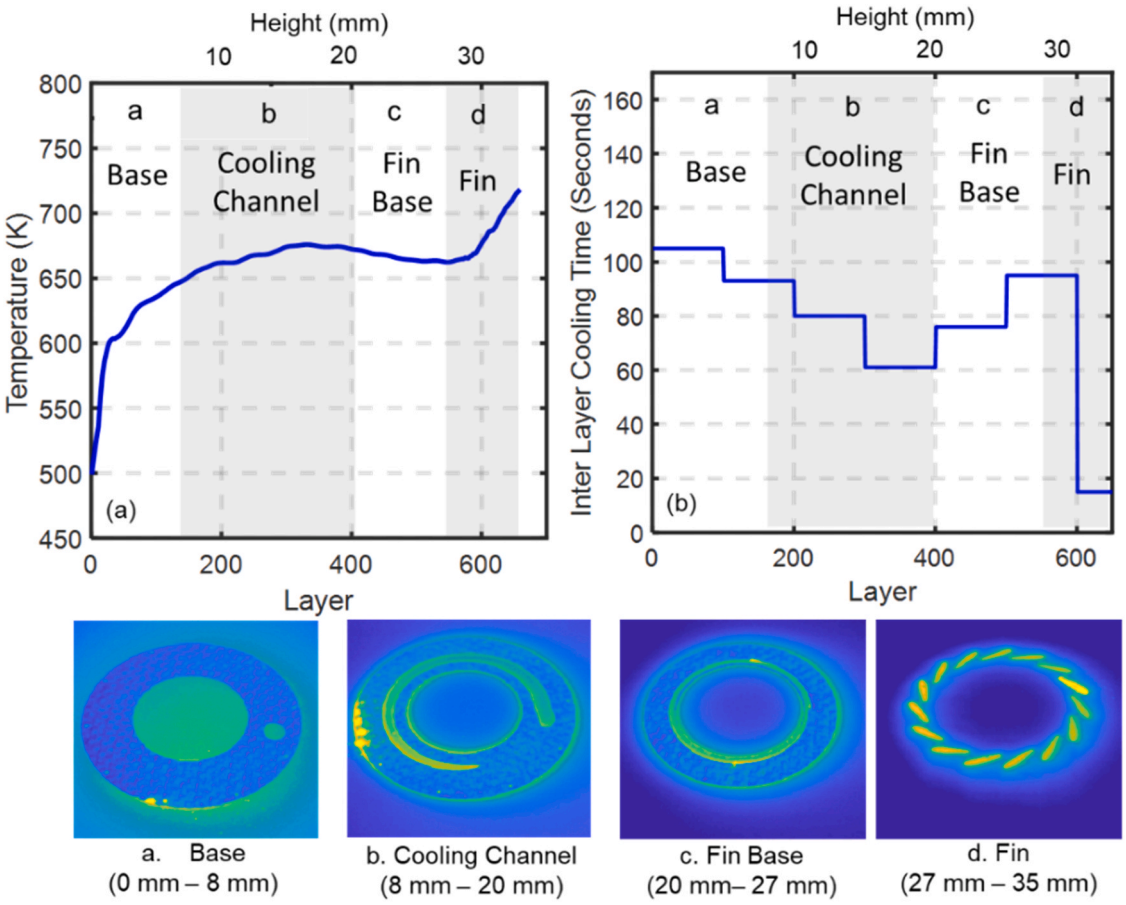

Fig. 8. (a) Steady state temperature of the top surface at each layer, (b) Interlayer cooling time (ILCT) as a function of the layer height. The ILCT is the time between layers. The ILCT is not constant, but is dependent on the surface area melted. The ILCT reduces drastically when processing the fin owing to the thin cross-section, which in turn leads to increase in temperature.

from solid to a liquid, and then back to a solid is not accounted in the graph theory approach.

- *Energy source-related assumptions.* The laser is considered a point heat source, i.e., the shape of the meltpool is not considered in the graph theory approach. For example, in the literature, Goldak's model from thermal modeling in welding is often scaled to LPBF [38]. Goldak's model assumes that the a double ellipsoid meltpool shape [40].

Furthermore, it was assumed that the topmost layer of the powder completely absorbed the incident laser beam. Hence, the graph theory approach ignored the effect of reflectivity and powder packing density.

The main computational bottleneck of the graph is in constructing the network graph, and obtaining the eigenvalues (Λ) and eigenvectors (ϕ) in Eq. (7). In what follows, we describe three strategies to represent the part geometry in the form of a discrete nodes, and subsequently, compute the eigenvectors (ϕ) and eigenvalues (Λ) of the Laplacian Matrix (L).

Of these three strategies, Strategy 1 involves populating the entire part with nodes. Strategy 2 takes advantage of the radial symmetry of the impeller to simulate a representative section of the geometry.

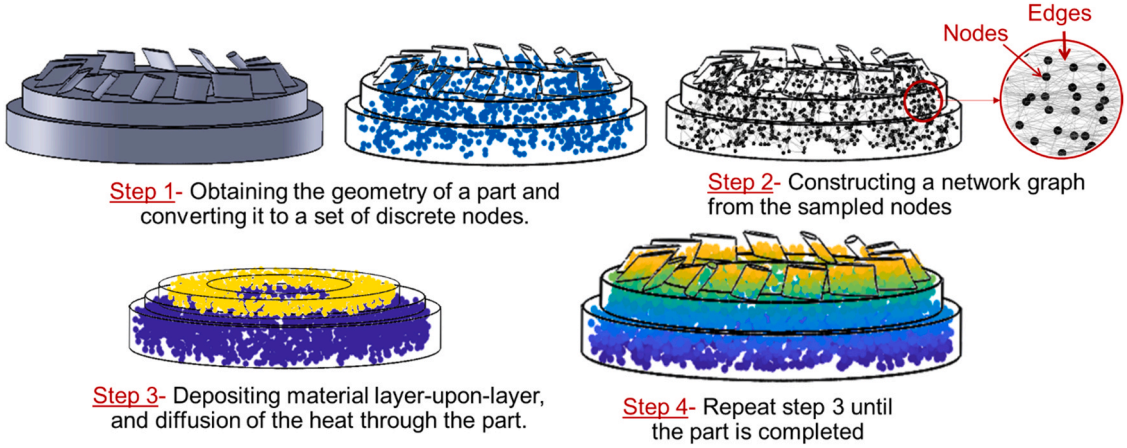

Fig. 9. Graph theory thermal modeling procedure steps for strategy 1.

Strategy 3 simulates large horizontal sub-sections of the part, one at a time, instead of the entire part, as in Strategy 1.

3.4. Strategy 1 – represent the entire part geometry as a network graph

3.4.1. Steps in the approach

Strategy 1 is depicted in Fig. 9, and was described in our previous publications [27,28]. We briefly reiterate the approach for the readers' convenience. The key idea is to solve the heat diffusion equation over a network graph constructed over a set of randomly sampled discrete nodes in the part using the concept outlined in Section 3.3.1. The graph theory approach consists of four steps, these are described herewith.

Step 1: Convert the entire part into a set of discrete number of nodes (n) that are randomly allocated through the part.

The part geometry is represented in the form of STL file in terms of vertices and edges. A number of n vertices is randomly sampled in each layer. These randomly sampled vertices are called nodes. The spatial position of these nodes is recorded in terms of their cartesian coordinates (x,y,z). In the ensuing steps, the temperature at each time step is stored at these nodes. The random sampling of the nodes bypasses the expensive meshing of FE analysis and is one of the key reasons for the reduced computational burden of the graph theory approach.

Step 2: Construct a network graph among randomly sampled nodes.

The procedure for constructing a network graph is described in the context of Fig. 10. Consider two nodes, π_i and π_j whose spatial Cartesian coordinates are $c_i \equiv (x_i, y_i, z_i)$ and $c_j \equiv (x_j, y_j, z_j)$. The Euclidean distance between π_i and a node π_j is $\|c_i - c_j\| = \sqrt{(x_i - x_j)^2 + (y_i - y_j)^2 + (z_i - z_j)^2}$. We connect two nodes if they are within l mm of each other called the *characteristic length*. The characteristic length is based on the geometry of the part and is set depending on the feature with the finest dimension of the part. The concept is that there should be no direct heat transfer between nodes that are physically far from each other. If two nodes π_i and π_j are within a radius of l, they are connected by an edge whose weight a_{ij} is given by,

$$a_{i,j} = e^{-\frac{\|c_i - c_j\|^2}{\sigma^2}} \quad \forall\ i \neq j \text{ and } \|c_i - c_j\| \leq l$$
$$a_{i,j} = 0, \qquad \text{otherwise} \tag{9}$$

The edge weight, a_{ij} represents the normalized strength of the connection between the nodes π_i and π_j and has a value between 0 and 1; σ^2 is the variation of the distance between all nodes that are connected to each other, i.e., within a radius of l. Thus, each node is connected to every node within a l neighborhood, but not to itself. In this work we set $l = 3$ mm corresponding to the finest feature of the impeller, viz., the fin section.

Next, we make the network graph sparse by removing some edges; we only connect a node to a certain number of its nearest neighboring nodes ($\eta = 5$ in this work). In other words, for a particular node, we remove edges farther (in terms of the Euclidean distance) than the nearest five by setting their edge weight to zero. The number of nearest neighbors (η) is calibrated from experiments from our previous work [27]. The sparsening of the network graph is advantageous for computational aspects.

From a physical perspective, the edge weight a_{ij} embodies the Gaussian law – called heat kernel — in the following manner. The closer a node π_i is to another π_j, exponentially stronger is the connection $(a_{i,j})$ and hence proportionally greater is the heat transfer between them.

A matrix is formed by placing a_{ij} in a row i and column j, this matrix is called the adjacency matrix, $A = [a_{i,j}]$.

$$A = \begin{bmatrix} 0 & a_{1,2} & a_{1,3} & \cdots & a_{1,N} \\ a_{2,1} & 0 & a_{2,3} & \cdots & a_{2,N} \\ a_{3,1} & a_{3,2} & 0 & \cdots & a_{3,N} \\ \vdots & \vdots & \vdots & \ddots & \vdots \\ a_{N,1} & a_{N,2} & a_{N,3} & \cdots & 0 \end{bmatrix} \tag{10}$$

The degree of node π_i is computed by summing the i^{th} row (column) of the adjacency matrix A.

$$d_i. = \sum_{\forall j} a_{i,j} \tag{11}$$

The diagonal degree matrix D is formed from $d_i.$'s as follows; where n is the number of nodes,

$$D = \begin{bmatrix} d_1. & \cdots & 0 \\ \vdots & \ddots & \vdots \\ 0 & \cdots & d_n. \end{bmatrix} \tag{12}$$

From the adjacency matrix (A) and degree matrix (D), the discrete graph Laplacian matrix L will be obtained using the following elementary matrix operations. the discrete Laplacian L can be cast in matrix form as,

$$L \quad \underline{\text{def}}(D - A)L = \begin{bmatrix} +d_1. & -a_{1,2} & -a_{1,3} & \cdots & -a_{1,N} \\ -a_{2,1} & +d_2. & -a_{2,3} & \cdots & -a_{2,N} \\ -a_{3,1} & -a_{3,2} & +d_3. & \cdots & -a_{3,N} \\ \vdots & \vdots & \vdots & \ddots & \vdots \\ -a_{N,1} & -a_{N,2} & -a_{N,3} & \cdots & +d_N. \end{bmatrix} \tag{13}$$

Finally, the Eigen spectra of the Laplacian L, computed using standard methods satisfy the following relationship:

$$L\phi = \phi\Lambda \tag{14}$$

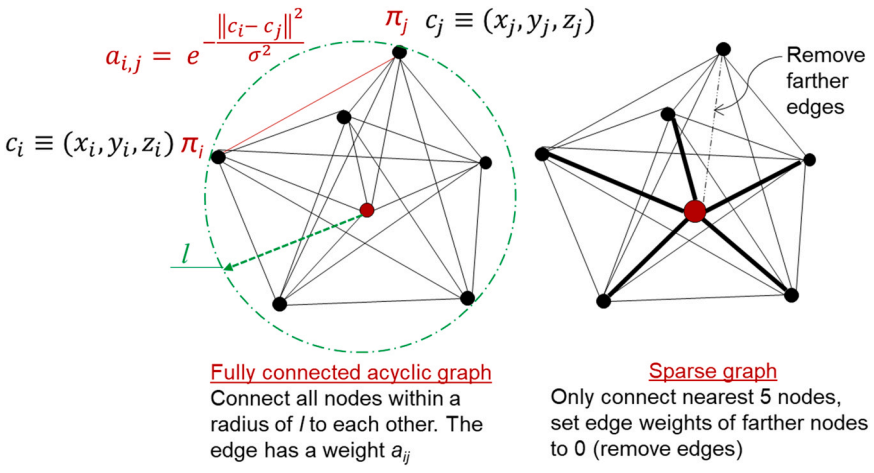

Fig. 10. Constructing a network graph over the part involves two aspects. First, connecting a node to all nodes with a radius l with an edge. Sparsening the graph by removing edges that are farther away than the nearest 5 nodes.

Because the matrix L is diagonally dominant with non-zero principal diagonal elements and negative off-diagonal elements it falls under a class of matrices called *Stieltjes matrix*. For such matrices the eigenvalues of L are non-negative ($\Lambda \geq 0$) and eigenvectors are orthogonal to each other ($\phi\phi^{T} = 1$).

Thus constructing the graph in the manner described in Eqs. (9)–(13) allows the heat diffusion equation to be solved as a superposition of the eigenvalues and eigenvectors of L as explained in the context of Eq. (7).

Step 3: Simulate the deposition of the entire layer and diffuse the heat throughout the network.

To aid computation, the simulation proceeds in the form of a superlayer (metalayer). In this work, we used 10 actual layers each of height 50 μm for one superlayer; the thickness of each superlayer was therefore 0.5 mm. An entire superlayer is assumed to be deposited at the melting point of the material T_0 (= 1600 K for SAE 316L). The superlayer or meta-layer approach was recently used by Hooper et al. for prediction of thermal-induced deformation [53]. Their work shows that the deformation predictions derived from a coarse meta-layer FE-based thermal model were within 20% of experimental observations [53].

By assuming that an entire layer is deposited at the melting point of the material, the graph theory approach ignores transient meltpool phenomena. To explain further, the meltpool temperature is considerably above the melting point of the material, and the transient meltpool aspects, such its instantaneous temperature and size are key determinants of the microstructure evolution [57]. The graph theory approach is therefore intended to capture the effects of part-level thermal history, such as distortion, cracking, delamination and failure of supports, and not the transient meltpool-related aspects, e.g., microstructure heterogeneity and granular-level solidification cracking.

The heat diffuses to the rest of the part below the current layer through the connections between the nodes. If the temperature at each node is arranged in matrix form, the steady state temperature T after time t (where t = interlayer cooling time) is obtained as a function of the eigenvectors (ϕ) and eigenvalues (Λ) of the Laplacian matrix (L) of the network graph, viz., Eq. (7), repeated herewith: $T(x, y, z, t) = \phi e^{-\alpha g \Lambda t} \phi' T_0$.

After the temperature of each node is obtained, convective and radiative thermal losses are included for the nodes on the top surface of each layer in Eq. (8).

Step 4: Step 3 is repeated until the part is built.

A new layer (s)of powder are deposited at the melting point T_0. The simulation of new powder layers is achieved by adding more nodes on top of existing nodes, akin to the element birth-and-death approach used in FE-based modeling of AM processes.

3.4.2. Limitations of Strategy 1

Strategy 1 is well-suited for relatively small volumes and simple geometries such as cylinders and cones, which were analyzed in our previous work [27]. There are two drawbacks with Strategy 1 which constrains its scalability for large volume parts with complex features. First, in Strategy 1 a fixed number of nodes are distributed in the part and are allocated randomly with uniform density. Consequently, certain features that have a thin cross section tend to have fewer nodes. For instance, the cross-sectional area of the fin-like features near the top of the part is considerably smaller than the rest of the part. Due to fewer nodes in the finer feature compared to the rest of the part, temperature distribution estimated in a fine feature will lack accuracy.

A second limitation from Strategy 1 is also caused by sparse distribution of nodes in fine features, such as the overhang section of the cooling channel and fins. Since the number of nodes in fine features is low, and a fixed number of nodes ($\eta = 5$) are connected to each other, the nodes in the fine feature regions tend to become connected to the nodes in the rest of the part across the boundary of the part and powder.

In other words, the edge connecting nodes may cross the boundary of the part, an occurrence termed as *short-circuiting*. Examples of short-circuiting are shown in Fig. 11. For instance, the edge connecting nodes should not cross the boundaries of the part or across the internal voids. An approach to avoid short-circuiting in Strategy 1 is to increase the node density, which will increase the computation time.

The third limitation of Strategy 1 is that it is computationally intensive. In Strategy 1, a large number of nodes for the entire part must be stored in the RAM memory of the desktop computer. Also, the Laplacian matrix (L) grows in size with the part. Consequently, the computation time increases as layers are added.

Moreover, at every time step it is necessary to keep track of the location and connectivity of every node over the entire part, as well as the Laplacian matrix (L), both of which scale as $\mathcal{O}^2(n)$ of the number of nodes (n). The number of eigenvalues (Λ) and eigenvectors (ϕ) also increases with the number of nodes. Consequently, the computation time for Strategy 1 scales exponentially with the number of nodes.

3.5. Strategy 2 - simulation a representative section of the part (part scaling)

In Strategy 2, instead of simulating the entire part, a radial section, or a sector, of the part is chosen for layer-by-layer analysis which is shown in Fig. 12. The graph thermal modeling steps are identical to the previous Strategy 1 which were described in Section 3.4.

The drawback with Strategy 2 is that it is best applied to symmetrical parts. However, simulating a section of a bigger part is a common practice in AM modeling to reduce the computational burden [32,62]. In our case, we chose a 24° sector as a representative section.

3.6. Strategy 3 – simulate the part in progressive horizontal subsections, and eliminate nodes in preceding subsections

Strategy 3 is designed to be a generalized approach to simulate any geometry. It overcomes the limitations of Strategy 1 by dividing the part into horizontal subsections and simulating each subsection in a progressive, piece-wise manner. As opposed to the naïve approach in Strategy 1, which populates the entire part with nodes, and stores the connections in large adjacency and Laplacian matrices, in Strategy 3, the key idea is to remove nodes in previous layers that lie far below the

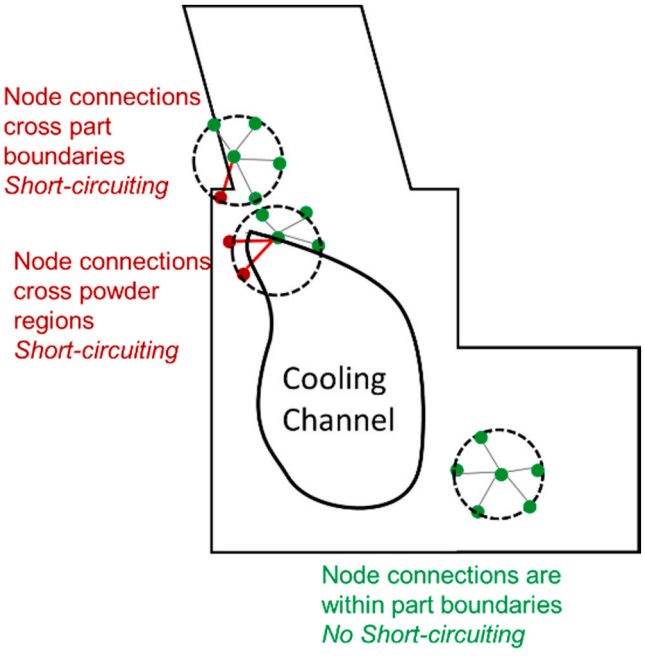

Fig. 11. Short-circuiting due to edges crossing the part boundaries and reaching across powder.

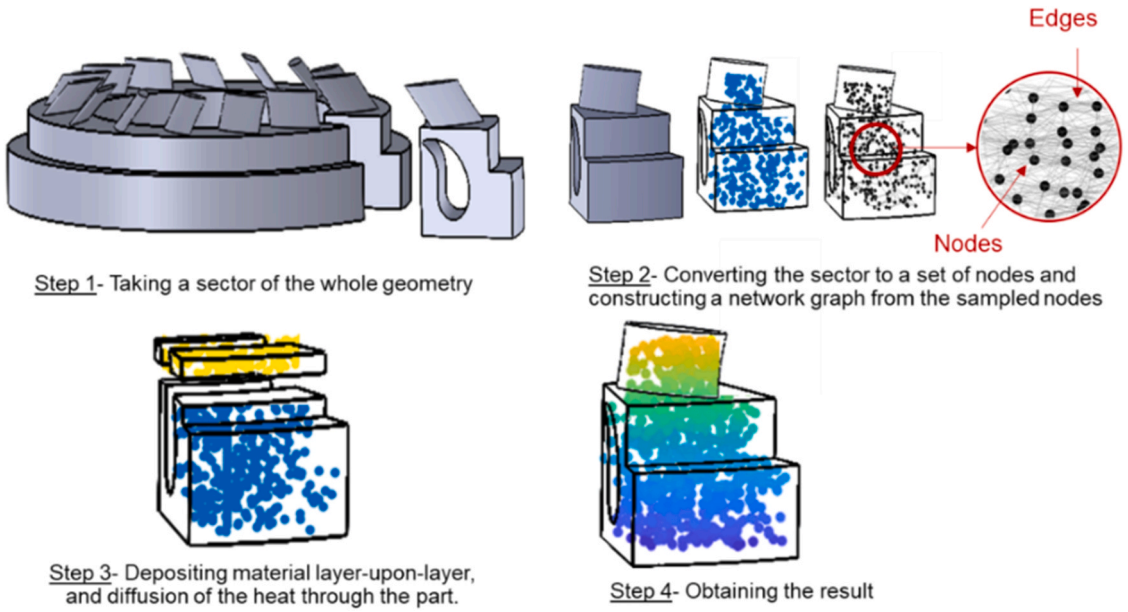

Fig. 12. Graph theory thermal modeling procedure steps for Strategy 2 involving simulation of a representative cross section of the part.

current layer being processed.

The rationale for removing nodes in previous layers is that the temperature cycles would be substantially attenuated by the time they reach deeper into the prior layers. This removal of nodes from previous layers not only overcomes the computational burden of Strategy 1, but also reduces inaccuracy as each sub-section can be populated with a large number of nodes. The following steps, also depicted in Fig. 13, summarize Strategy 3.

3.6.1. *Steps in the approach*

Step 1 – Use Strategy 1 with sparse nodes to obtain a coarse estimate of the thermal history.

A coarse estimate of the temperature trends for the whole part is obtained using Strategy 1 with reduced node density. The purpose of this step is to provide a rough estimate of each layer's thermal history at each time step which will be used at later Step 4.

Step 2 – The part is divided into smaller horizontal subsections (layerwise partitioning).

The part is divided into horizontal subsections, and each subsection is populated with discrete nodes and a network graph is created over each subsection. Each subsection has its own network graph, hence, there are no edges connecting the two adjacent subsections. The height of the sub-section is dictated by the maximum size of the Laplacian matrix that can be stored in the memory of the computer. In our case, the maximum size of the Laplacian matrix that could be stored at any time in memory corresponded to a height of 10 mm of the part.

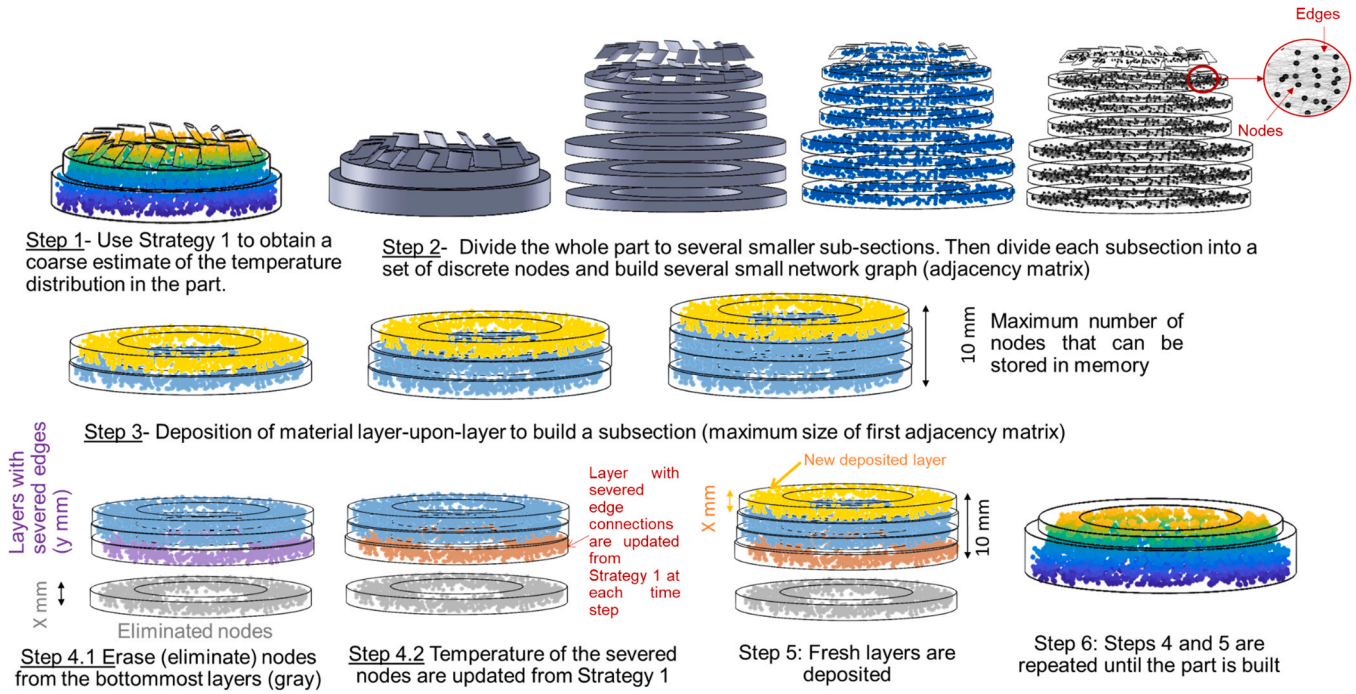

Fig. 13. Graph theory procedure steps for Strategy 3.

Step 3 – Simulate the deposition of material layer by layer for the first subsection.

The layers were deposited to reach the maximum size of the Laplacian matrix (10 mm height).

Step 4 – Remove nodes in previous subsections.

After the simulation of the first subsection is finished (10 mm), the computer memory is cleared (nodes must be erased), and the temperature of nodes with severed connections is estimated based on Step 1. This is done in two sub-steps.

Step 4.1: Nodes representing the first few layers of the previous subsection are removed. The removal of nodes reduces the size of the Laplacian matrix, and the number of nodes stored in memory. For example, the first 4 mm of the previous sub-section are removed, and thus there is now space in the computer memory to accommodate 4 mm of new layers to be deposited. The height of the erased nodes is termed as *moving distance*.

Step 4.2: The removal of nodes causes edge connections to be severed, which changes the topology of the network. One effect of removing nodes is that heat tends to accumulate in the nodes with edges connected to the erased nodes due to disconnection of the network graph. The available initial layers nodes with severed edges are termed *interface nodes*. The temperature of the interface nodes is reinitiated at each time step based on the coarse estimates from Step 1. In this work the interface nodes were 3 superlayer thickness (1.5 mm).

Step 5 – Simulate the deposition of a new subsection.

Fresh layers in the next sub-section are added until the maximum number of layers that can be stored in memory is reached. In this work fresh layers corresponding to an added 4 mm in height (80 actual layers, 8 superlayers) were deposited until an incremental height of 10 mm was reached (200 actual layers).

Step 6 - Step 4 and Step 5 are cycled until the part is completely built.

3.6.2. Limitations of Strategy 3

The advantage of Strategy 3 is that the computation time is significantly reduced compared to Strategy 1, and the approach can be generalized to any shape. However, a trade-off is that the temperature history of the eliminated nodes cannot be tracked for the entire process. tradeoff can be mitigated by setting the moving distance to a smaller value. However, since the eliminated nodes are significantly below the current layers (10 mm in our case), the temperatureat these eliminated nodes would have reached the steady state.

3.7. Simulation parameters

The graph theory approach requires tuning of three parameters — namely, the number of nodes in the volume simulated (n), the number of nodes to which each node is connected (η), and the gain factor (g) in Eq. (7) which controls the rate of heat diffusion through the nodes. In this work, we set $\eta = 5$ and $g = 1.5 \times 10^4$. The number of nearest neighbors η and gain factor g were calibrated in our previous work and described in depth in Ref. [27]. We did not change these already calibrated parameters from our previous work in LPBF of stainless steel parts which substantiates that the graph theory approach only needs to be calibrated once via pilot experiments for a specific material [27].

The graph theory simulation parameters and material properties are described in Table 2. Also included in Table 2 is a term called characteristic length (l, mm). In our previous works, the characteristic length (l) was defined as the distance beyond which there should not be any physical connection between nodes to avoid short-circuiting, and was estimated by measuring the minimum dimension of various features in the part. In this work, the thickness of the fin (~3 mm) was one of the smallest dimensions, albeit, certain sections of the cooling channels were thinner.

Hence, as a rule of thumb we maintained $l = 3$ mm. The characteristic length (l) also facilitates estimation of the minimum number of nodes (n), as a function of the number of neighbors ($\eta = 5$) and volume (V) of the geometry simulated via the following relationship:

$$n = \frac{\eta \times V}{l^3} = \frac{5V}{27} \tag{15}$$

Two metrics were used to assess the accuracy and precision of the graph theory approach, namely, the mean absolute percentage error (MAPE) and root mean square error (RMSE), shown in Eqs. (15a) and (15b), respectively.

$$\text{MAPE} = \frac{100}{k} \times \sum_{i=1}^{k} \left| \frac{T_i - \widehat{T}_i}{T_i} \right| \tag{15a}$$

$$\text{RMSE} = \sqrt{\sum_{i=1}^{k} \frac{\left(T_i - \widehat{T}_i\right)^2}{k}} \tag{15b}$$

where k is the number of instances in time that were compared over the duration of the deposition, i is the current instant of time, T_i is the measured temperature, and $\widehat{T}_i$ is the predicted temperature.

Table 2
Summary of the simulation parameters used in this work.

Simulation parameters	Values
Heat loss coefficient from part to surroundings, $\tilde{h}$ [W m^{-2} K]	1×10^{-5} (Ref. [27])
Heat loss coefficient from part to substrate (sink), $\tilde{h}$ [W m^{-2} K]	1×10^{-2} (Ref. [27])
Thermal diffusivity (α), [m^2/s]	3×10^{-6}
Density, ρ [kg/m^3]	8440
Melting Point (T_0) [K]	1600
Ambient temperature, T_∞ [K]	300
Characteristic length [mm]	3
Number of neighbors which is connected to each node (η)	5
Superlayer thickness [mm]	0.5 (10 actual layers)
Gain factor (g)	1.5×10^4
Computational hardware	AMD Ryzen Threadripper 3970X, @3.7 GHz with 128 GB RAM.
Computation Software	MATLAB2020a

4. Results and discussion

4.1. Strategy 1

Fig. 14 and Table 3 report results for Strategy 1 in terms of mean absolute percentage error (MAPE), root mean square error (RMSE, [K]), and computational time as a function of number of nodes. The volume of the whole part V was ~250,000 mm^3, which requires a minimum of $n = 46{,}000$ nodes based on Eq. (14). From a computational standpoint, the Laplacian and adjacency matrix will each consist of over 2×10^9 elements (46,000 rows × 46,000 columns). Furthermore, 46,000 eigenvalues and eigenvectors will have to be computed.

Strategy 1 resulted in ~14% MAPE and 47 K RMSE with 64,000 nodes, and required 10.5 h of computation time. The desktop computer used in this work had 128 gigabytes of memory with maximum capacity of ~70,000 nodes. Therefore, increasing the number of nodes beyond 64,000 overwhelmed the memory of the desktop computer.

While Strategy 1 captures the overall trend in steady state temperature distribution, the prediction error is large for sections with the internal channel and fins. The main reason for this large error is due to short-circuiting of edges across the cooling channel and between the fin and bulk part as depicted in Fig. 11. Accordingly, a large number of nodes are need for Strategy 1, an alternative is to thread the computation through a GPU using a compiled language, such as C++.

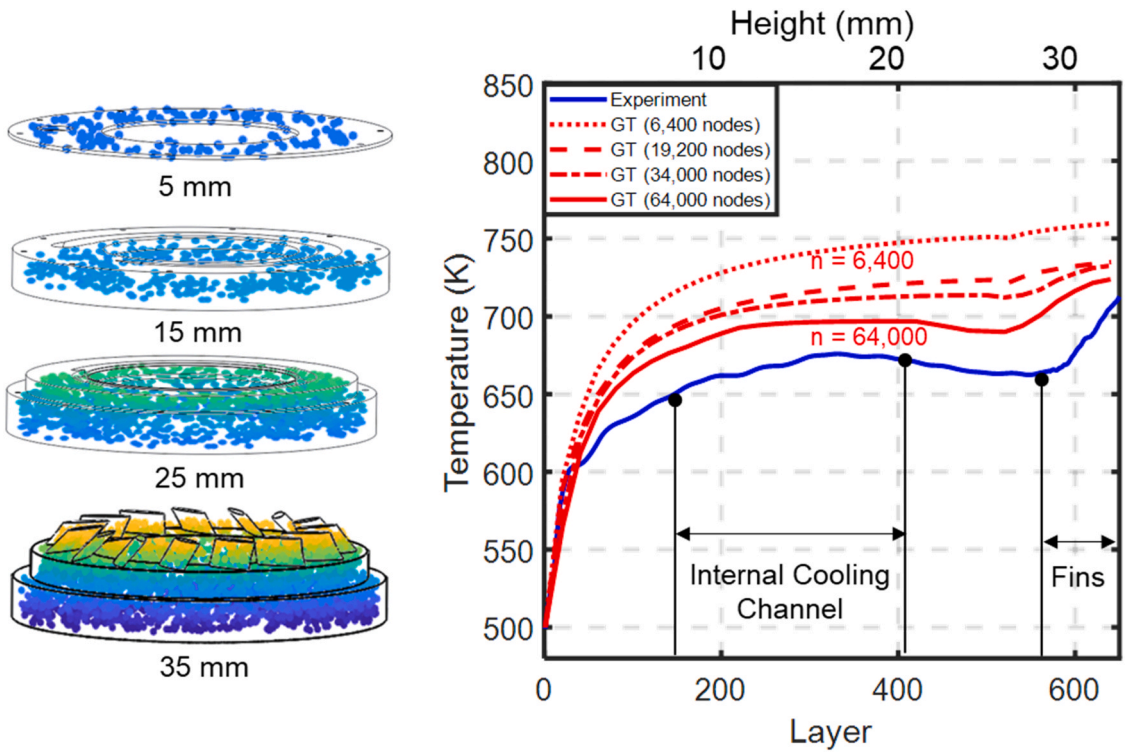

Fig. 14. Comparison of the predicted top surface temperature from Strategy 1 with experimentally observed temperature distribution as a function of number of nodes (n).

Table 3
Comparison of strategy 1 accuracy and computational time for different node densities.

Number of nodes (n)	MAPE (Std. Dev. over three repetitions)	RMSE (Std. Dev. over three repetitions) [K]	Time (minutes)
3200	55.2 (4.7)	170.4 (19.8)	2
6400	36.1 (2.6)	110.8 (12.7)	6
9600	26.7 (2.3)	91.2 (10.2)	16
19,200	25.4 (1.9)	89.6 (8.6)	39
25,600	22.8 (2.1)	68.4 (8,2)	53
34,000	14.7 (1.9)	53.7 (7.5)	236
64,000	13.6 (1.8)	46.2 (7.4)	634

The number in the parenthesis indicates the uncertainty (standard deviation) over three independent replications.

4.2. Strategy 2

In Strategy 2, a representative radial slice of the part is simulated. The results for Strategy 2 are shown in Fig. 15 and Table 4. Since the volume of the sector chosen (31,000 mm^3) is a fraction of the entire part volume (250,000 mm^3), the sector can be more densely populated with nodes compared to Strategy 1, providing more accurate results with fewer number of nodes.

For Strategy 2, from Eq. (14), it was estimated that $n = 5800$ and above would be needed to capture the trends. Indeed, with 6000 nodes, the thermal trends were predicted with MAPE ~10%, RMSE 33 K in less than 5 min. There is a diminishing return on the accuracy with increase in number of nodes. With 24,000 nodes, the graph theory approach required about 40 min to converge to a MAPE and RMSE of 3.5% and 11.8 K, respectively. A tradeoff is at 11,200 nodes, for which the simulation converges to 8.6% (MAPE) and 29 K (RMSE) in less than 18 min.

We also compared the graph theory solution with a FE analysis, based on the pragmatic approach described by Hooper et al. [53]. As reported in Fig. 15 and Table 4, to reach a similar level of MAPE

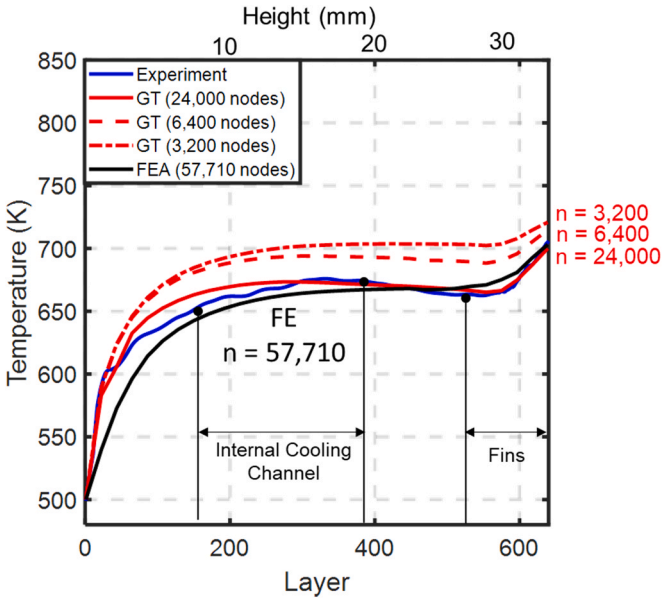

Fig. 15. Results from using strategy 2 to simulate a sector of the part layer by layer as a function of the number of nodes. With n = 24,000, the graph theory predictions converge to within 3.5% (MAPE) and 12 K (RMSE) of the experimental measurements within 41 min. The FE approach requires 57,710 nodes for a 9% MAPE and 29 K RMSE, and converged in 273 min (4.5 h).

(< 9%) and RMSE (< 30 K), the graph theory approach used 11,200 nodes and required 17 min of computation to converge, while the FE analysis requires, respectively, 57,710 nodes and 273 min. A qualitative comparison of the FE and graph theory solutions is depicted in Fig. 16.

Table 4
Comparison of strategy 2 accuracy and computational time for different node densities.

Graph theory			
Nodes	MAPE (Std. Dev. over three repetitions)	RMSE (Std. Dev. over three repetitions) [K]	Time (min)
38,000	3.4 (0.3)	11.6 (2.0)	106
24,000	3.5 (0.3)	11.8 (2.4)	41
12,800	7.9 (0.6)	27.5 (3.6)	21
11,200	8.6 (0.9)	28.1 (3.2)	17
9600	9.1 (0.9)	30.0 (4.1)	14
6400	10.1 (1.1)	33.2 (4.9)	5
Finite element			
Nodes	MAPE (Std. Dev. over three repetitions)	RMSE (Std. Dev. over three repetitions) [K]	Time (min)
57,710	8.4	29.4	273

The number in the parenthesis indicates the uncertainty (standard deviation) over three independent replications.

4.3. Strategy 3

The results for Strategy 3 are reported in Table 5 and Fig. 17. In Table 5 we summarize results from varying the moving distance (height of nodes eliminated), and different number of nodes used for the coarse estimation of temperature at the interface nodes in Step 1 of the approach.

The minimum number of nodes per subsection of 10 mm was estimated from Eq. (14) as follows. The finest feature, prone to short-circuiting are the fin-shaped features, whose total volume amounted to $V = 26{,}500\ mm^3$. with characteristic length $l = 3$ mm, and the number of neighboring nodes $\eta = 5$, the number of nodes to avoid short-circuiting in the fin section of the part was estimated as $n = 5000$.

With $n = 5000$, and moving distance set at 2 mm and lesser, Strategy 3 predicted the top surface temperature with error within 10% (MAPE) and 35 K (RMSE) in approximately 20 min. Doubling the number of nodes in each subsection to $n = 10{,}000$, and maintaining the same moving distance resulted in reduction of MAPE to ~8%, and RMSE less than 25 K.

Fig. 17 shows that Strategy 3 captured the subtle temperature trends characteristic of the internal cooling channel and fins. The moving distance impacts the prediction error; a shorter moving distance entails that fewer nodes are removed, and hence there is a smoother transition between each subsection. A smaller moving distance, however, increases the computational time as more nodes are needed to be stored in memory. The total computation time reported in Table 5 includes the time required for coarse estimation using Strategy 1.

4.4. Qualitative comparison with Netfabb

Here we provide a qualitative comparison of the graph theory results with a commercial AM simulation software Autodesk Netfabb. As described in Section 2.1, commercial simulation packages, including Netfabb, use a proprietary approach for adaptive meshing. The user cannot control the number of elements in Netfabb except to choose between three simulation modes labeled fastest, medium, and accurate. Accordingly, it is not possible to interrogate the temperature at specific locations. Therefore, a one-to-one quantitative comparison of Netfabb and graph theory predictions cannot be made. Hence, the following comparison of the Netfabb solution with the graph theory is intended to be only qualitative in nature. We have carried out such a comparison with non-proprietary FE, finite difference, and exact analytical solutions in our prior publications [27–29], as well is in Section 4.3 vis-à-vis Strategy 2.

Results from Strategy 1 ($n = 19{,}200$) and Strategy 2 ($n = 12{,}800$) are qualitatively compared with graph theory at specific build heights in Fig. 18. The graph theory results and Netfabb simulations both predicted heat accumulation in the fin region, and fast diffusion in the annulus. For both scenarios, the Netfabb simulation was set on the fastest mode.

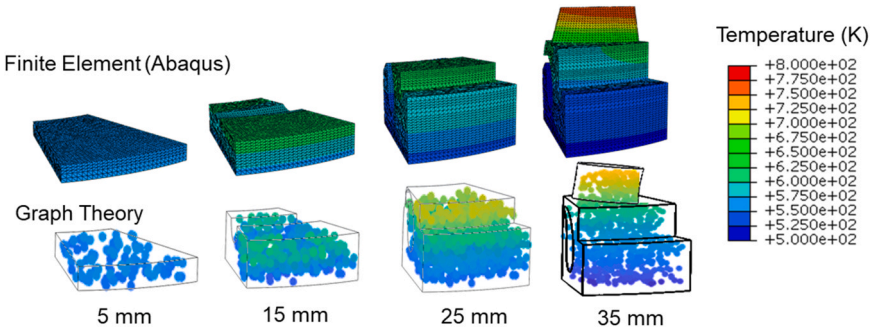

Fig. 16. Qualitative comparison of the graph theory and finite element solution for Strategy 2. The graph theory approach requires about 1/5th of the time of FE analysis (using the DFLUX routine in Abacus) to provide a similar level of accuracy.

Table 5
Results from applying strategy 3 with different node densities and window size.

Moving distance	Number of nodes (n) for coarse estimation (Step 1)	Nodes in each sub-section in Step 2	MAPE (Std. Dev. over three repetitions)	RMSE (Std. Dev. over three repetitions) [K]	Computation time for coarse estimation (Step 1) (min)	Computation time for Steps 4 and 5 (min)	Total Time (min)
8 mm	6400	5000	43.5 (4.1)	117.2 (16.8)	6	5	11
5 mm			16.9 (3.5)	64.2 (7.7)		7	13
2 mm			9.5 (0.8)	30.5 (4.8)		11	17
1 mm			8.1 (0.9)	25.7 (3.8)		16	22
8 mm		10,000	41.8 (3.7)	109.3 (13.5)		9	15
5 mm			15.3 (2.8)	60.4 (7.2)		15	21
2 mm			7.9 (0.8)	23.8 (4.0)		21	27
1 mm			6.1 (0.8)	22.7 (3.7)		33	39

The number in the parenthesis indicates the uncertainty (standard deviation) over three independent replications.

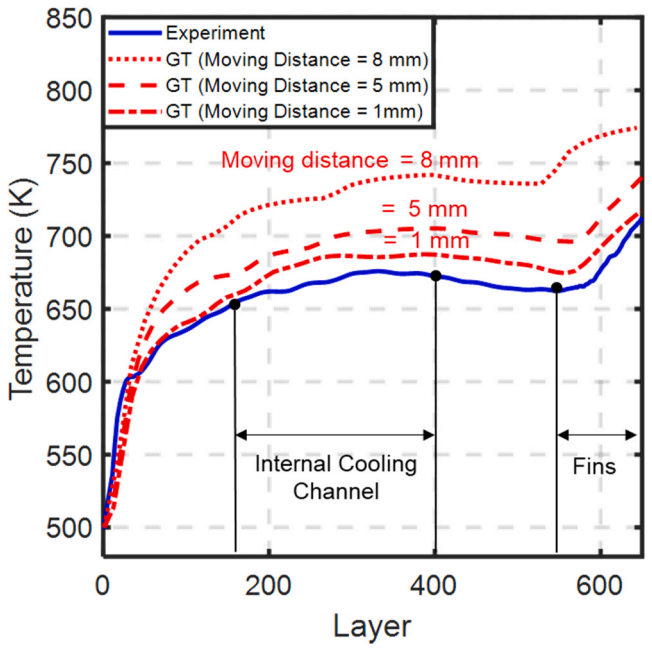

Fig. 17. Comparing the experimental top surface temperature with the predicted top surface temperature for Strategy 3 at a constant number of nodes, n = 10,000.

5. Conclusions and future work

This work scales the graph theory approach for predicting the thermal history of a large stainless steel impeller part made using the laser powder bed fusion process (LPBF). The impeller had an outside diameter of 155 mm and a vertical height of 35 mm (250,000 mm^3). The part was built on a Renishaw AM250 commercial LPBF system, and required the melting of 700 layers over 16 h of build time. During the build, temperature readings of the top surface of the part were acquired using an infrared thermal camera operating in the longwave infrared range (7–13 μm). This work validated three computational strategies to scale the graph theory approach, with the aim of reducing the prediction time to less than the actual time to print the part.

Strategy 1 involved populating the entire part with nodes and constructing a network graph over these nodes. This strategy was used in our previous works for small parts and is found to be computationally intensive for large parts as many graph nodes have to be stored in memory. For simulating the impeller part using Strategy 1, the best result was obtained in 10.5 h and required 64,000 nodes; the mean absolute percentage error (MAPE) and root mean square error (RMSE) were ~14% and 47 K, respectively.

Strategy 2 scaled the part geometry by simulating a small representative radial cross section of the impeller. With 6400 nodes, the Strategy 2 resulted in a MAPE ~10% and RMSE 32 K within 5 min of computation. However, this approach is suitable for symmetrical parts. Doubling the number of nodes to 12,800 reduces the MAPE and RMSE to ~8% and 27.5 K, at the cost of computation time, which increases to ~22 min.

Strategy 3 used a moving window approach to simulate the thermal history in horizontal subsections. Instead of discretizing the entire part into nodes and building a large network graph to cover all the nodes in the part as in Strategy 1, the part in Strategy 3 was divided into horizontal subsections. The thermal history of the part was progressively predicted subsection-by-subsection, and to keep the computation tractable and avoid overwhelming the memory of the computer, the nodes in prior subsections were removed. With number of nodes set at 5000 per section, this strategy resulted in a MAPE less than 10% and RMSE less than 30 K within 25 min of simulation. The MAPE and RMSE decreased slightly to ~8% and 25 K when the number of nodes was doubled to 10,000, at the cost of computation time, which increased from 30 to 40 min.

This work thus succeeds in instituting an efficient approach to deploy the graph theory-based thermal modeling for predicting the temperature distribution in large volume and complex-shaped LPBF parts designed for practical applications. The future work is to make the graph theory approach more efficient through code parallelization and optimization.

We aim to leverage the graph theory approach in our future works for both prediction and prevention of build failures in LPBF. An avenue being explored is to fuse the thermal history predictions from graph theory with real-time in-process sensor data in a machine learning model to predict flaw formation [63].

CRediT authorship contribution statement

Reza Yavari: Conceptualization, Methodology, Software, Validation, Formal analysis, Data curation, Writing - original draft,

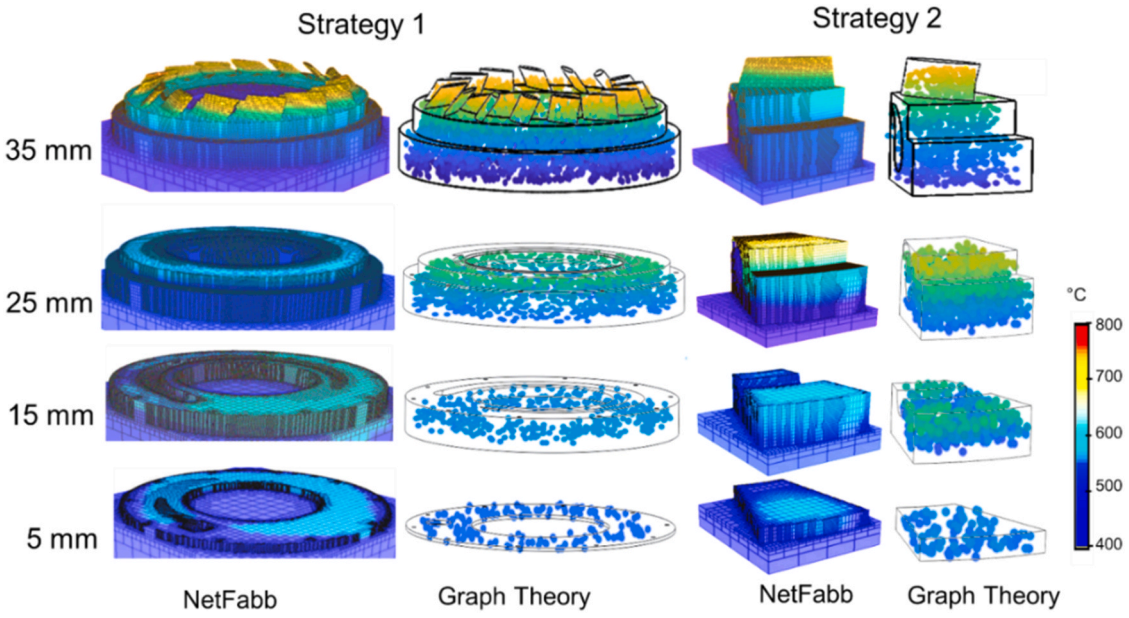

Fig. 18. Qualitative comparison of the graph theory approach with Netfabb shows similar trends. Note the prominent heat accumulation in the fin region.

Visualization; **Richard Williams**: Investigation, Data Curation; **Alex Riensche**: Visualization, Software; **Paul A. Hooper**: Resources, Investigation, Data curation, Supervision, Writing - review & editing; **Kevin D. Cole**: Conceptualization, Methodology, Writing - original draft, Writing - review & editing, Supervision; **Lars Jacquemetton**: Writing - review & editing; **Harold (Scott) Halliday**: Writing - review & editing; **Prahalada Krishna Rao** : Conceptualization, Methodology, Resources, Writing - original draft, Writing - review & editing, Supervision, Project administration, Funding acquisition.

Declaration of Competing Interest

The authors declare that they have no known competing financial interests or personal relationships that could have appeared to influence the work reported in this paper.

Acknowledgements

Prahalada Rao thanks the United States National Science Foundation (NSF) for funding his work under awards OIA-1929172, CMMI-1719388, CMMI-1920245, CMMI-1739696, and CMMI-1752069, and the United States Department of Energy DE-SC0021136. Predicting the thermal history of LPBF parts was the major aspect of CMMI-1752069 (Program Officer: Kevin Chou). Supplemental funding for CMMI-1752069 obtained through the NSF INTERN program (Program Officer: Prakash Balan) and CMMI Data Science Activities (Program Officer: Martha Dodson) is greatly appreciated. The former NSF INTERN supplement funded a large part of Reza Yavari's research. Improvements to the graph theory algorithm were proposed in DE-SC0021136. The authors thank Autodesk for providing an academic license of their Netfabb software. Scott Halliday thanks the NSF for funding the Navajo Technical University Center for Advanced Manufacturing via HRD-1840138.

References

[1] M. Schmidt, M. Merklein, D. Bourell, D. Dimitrov, T. Hausotte, K. Wegener, L. Overmeyer, F. Vollertsen, G.N. Levy, Laser based additive manufacturing in industry and academia, CIRP Ann. 66 (2) (2017) 561–583, https://doi.org/10.1016/j.cirp.2017.05.011.

[2] O. Diegel, A. Nordin, D. Motte, A Practical Guide to Design for Additive Manufacturing, Springer, Singapore, 2019.

[3] C. Dordlofva, O. Borgue, M. Panarotto, O. Isaksson, Drivers and guidelines in design for qualification using additive manufacturing in space applications, Proc. Des. Soc. Int. Conf. Eng. Des. 1 (1) (2019) 729–738, https://doi.org/10.1017/dsi.2019.77.

[4] A. du Plessis, I. Yadroitsava, I. Yadroitsev, Effects of defects on mechanical properties in metal additive manufacturing: a review focusing on X-ray tomography insights, Mater. Des. 187 (2020), 108385, https://doi.org/10.1016/j.matdes.2019.108385.

[5] Z. Snow, A.R. Nassar, E.W. Reutzel, Invited review article: review of the formation and impact of flaws in powder bed fusion additive manufacturing, Addit. Manuf. 36 (2020), 101457, https://doi.org/10.1016/j.addma.2020.101457.

[6] R.J. Williams, A. Piglione, T. Rønneberg, C. Jones, M.-S. Pham, C.M. Davies, P. A. Hooper, In situ thermography for laser powder bed fusion: Effects of layer temperature on porosity, microstructure and mechanical properties, Addit. Manuf. 30 (2019), 100880, https://doi.org/10.1016/j.addma.2019.100880.

[7] T. DebRoy, H.L. Wei, J.S. Zuback, T. Mukherjee, J.W. Elmer, J.O. Milewski, A. M. Beese, A. Wilson-Heid, A. De, W. Zhang, Additive manufacturing of metallic components – process, structure and properties, Prog. Mater. Sci. 92 (2018) 112–224, https://doi.org/10.1016/j.pmatsci.2017.10.001.

[8] W.J. Sames, F. List, S. Pannala, R.R. Dehoff, S.S. Babu, The metallurgy and processing science of metal additive manufacturing, Int. Mater. Rev. 61 (5) (2016) 315–360.

[9] M. Seifi, A. Salem, J. Beuth, O. Harrysson, J.J. Lewandowski, Overview of materials qualification needs for metal additive manufacturing, JOM 68 (3) (2016) 747–764.

[10] B. Dovgyy, A. Piglione, P.A. Hooper, M.-S. Pham, Comprehensive assessment of the printability of CoNiCrFeMn in laser powder bed fusion, Mater. Des. 194 (2020), 108845, https://doi.org/10.1016/j.matdes.2020.108845.

[11] E. Atzeni, A. Salmi, Study on unsupported overhangs of AlSi10Mg parts processed by Direct Metal Laser Sintering (DMLS), J. Manuf. Process. 20 (2015) 500–506, https://doi.org/10.1016/j.jmapro.2015.04.004.

[12] B. Cheng, K. Chou, Deformation evaluation of part overhang configurations in electron beam additive manufacturing, ASME 2015 International Manufacturing Science and Engineering Conference, American Society of Mechanical Engineers, (2015) p. V001T002A072.

[13] J.C. Fox, S.P. Moylan, B.M. Lane, Effect of process parameters on the surface roughness of overhanging structures in laser powder bed fusion additive manufacturing, Procedia CIRP 45 (2016) 131–134.

[14] J.P. Oliveira, A.D. LaLonde, J. Ma, Processing parameters in laser powder bed fusion metal additive manufacturing, Mater. Des. 193 (2020), 108762, https://doi.org/10.1016/j.matdes.2020.108762.

[15] F. Imani, A. Gaikwad, M. Montazeri, P. Rao, H. Yang, E. Reutzel, Process mapping and in-process monitoring of porosity in laser powder bed fusion using layerwise optical imaging, J. Manuf. Sci. Eng. 140 (10) (2018), https://doi.org/10.1115/1.4040615.

[16] J.P. Oliveira, T.G. Santos, R.M. Miranda, Revisiting fundamental welding concepts to improve additive manufacturing: from theory to practice, Prog. Mater. Sci. 107 (2020), 100590, https://doi.org/10.1016/j.pmatsci.2019.100590.

[17] J.J. Lewandowski, M. Seifi, Metal additive manufacturing: a review of mechanical properties, Annu. Rev. Mater. Res. 46 (1) (2016) 151–186, https://doi.org/10.1146/annurev-matsci-070115-032024.

[18] C.S. Lough, X. Wang, C.C. Smith, R.G. Landers, D.A. Bristow, J.A. Drallmeier, B. Brown, E.C. Kinzel, Correlation of SWIR imaging with LPBF 304L stainless steel part properties, Addit. Manuf. 35 (2020), 101359, https://doi.org/10.1016/j.addma.2020.101359.

[19] M. Gorelik, Additive manufacturing in the context of structural integrity, Int. J. Fatigue 94 (2017) 168–177, https://doi.org/10.1016/j.ijfatigue.2016.07.005.

[20] H.L. Wei, T. Mukherjee, W. Zhang, J.S. Zuback, G.L. Knapp, A. De, T. DebRoy, Mechanistic models for additive manufacturing of metallic components, Prog. Mater. Sci. (2020), 100703, https://doi.org/10.1016/j.pmatsci.2020.100703.

[21] P.C. Collins, C.V. Haden, I. Ghamarian, B.J. Hayes, T. Ales, G. Penso, V. Dixit, G. Harlow, Progress toward an integration of process–structure–property–performance models for "Three-Dimensional (3-D) Printing" of titanium alloys, JOM 66 (7) (2014) 1299–1309, https://doi.org/10.1007/s11837-014-1007-y.

[22] P. Foteinopoulos, A. Papacharalampopoulos, P. Stavropoulos, On thermal modeling of additive manufacturing processes, CIRP J. Manuf. Sci. Technol. 20 (2018) 66–83, https://doi.org/10.1016/j.cirpj.2017.09.007.

[23] Z. Luo, Y. Zhao, A survey of finite element analysis of temperature and thermal stress fields in powder bed fusion additive manufacturing, Addit. Manuf. 21 (2018) 318–332, https://doi.org/10.1016/j.addma.2018.03.022.

[24] A. Banadyopadhyay, K.D. Traxel, Invited review article: metal-additive manufacturing—modeling strategies for application-optimized designs, Addit. Manuf. 22 (2018) 758–774, https://doi.org/10.1016/j.addma.2018.06.024.

[25] B. Schoinochoritis, D. Chantzis, K. Salonitis, Simulation of metallic powder bed additive manufacturing processes with the finite element method: a critical review, Proc. Inst. Mech. Eng. Part B J. Eng. Manuf. 231 (1) (2015) 96–117, https://doi.org/10.1177/0954405414567522.

[26] N. Peter, Z. Pitts, S. Thompson, A. Saharan, Benchmarking build simulation software for laser powder bed fusion of metals, Addit. Manuf. 36 (2020), 101531, https://doi.org/10.1016/j.addma.2020.101531.

[27] R. Yavari, R.J. Williams, K.D. Cole, P.A. Hooper, P. Rao, Thermal modeling in metal additive manufacturing using graph theory: experimental validation with in-situ infrared thermography data from laser powder bed fusion, J. Manuf. Sci. Eng. (2020) 1–43, https://doi.org/10.1115/1.4047619.

[28] M.R. Yavari, K.D. Cole, P. Rao, Thermal modeling in metal additive manufacturing using graph theory, J. Manuf. Sci. Eng. 141 (7) (2019), https://doi.org/10.1115/1.4043648.

[29] K.D. Cole, M.R. Yavari, P.K. Rao, Computational heat transfer with spectral graph theory: quantitative verification, Int. J. Therm. Sci. 153 (2020), 106383, https://doi.org/10.1016/j.ijthermalsci.2020.106383.

[30] Z. Yan, W. Liu, Z. Tang, X. Liu, N. Zhang, M. Li, H. Zhang, Review on thermal analysis in laser-based additive manufacturing, Opt. Laser Technol. 106 (2018) 427–441, https://doi.org/10.1016/j.optlastec.2018.04.034.

[31] F. Hajializadeh, A. Ince, Finite element–based numerical modeling framework for additive manufacturing process, Mater. Des. Process. Commun. 1 (1) (2019), e28, https://doi.org/10.1002/mdp2.28.

[32] M. Gouge, E. Denlinger, J. Irwin, C. Li, P. Michaleris, Experimental validation of thermo-mechanical part-scale modeling for laser powder bed fusion processes, Addit. Manuf. 29 (2019), 100771, https://doi.org/10.1016/j.addma.2019.06.022.

[33] K. Zeng, D. Pal, H.J. Gong, N. Patil, B. Stucker, Comparison of 3DSIM thermal modelling of selective laser melting using new dynamic meshing method to ANSYS, Mater. Sci. Technol. 31 (8) (2015) 945–956, https://doi.org/10.1179/1743284714Y.0000000703.

[34] A. Olleak, Z. Xi, Scan-wise adaptive remeshing for efficient LPBF process simulation: the thermal problem, Manuf. Lett. 23 (2020) 75–78, https://doi.org/10.1016/j.mfglet.2020.01.003.

[35] P. Michaleris, Modeling metal deposition in heat transfer analyses of additive manufacturing processes, Finite Elem. Anal. Des. 86 (2014) 51–60, https://doi.org/10.1016/j.finel.2014.04.003.

[36] E.R. Denlinger, M. Gouge, J. Irwin, P. Michaleris, Thermomechanical model development and in situ experimental validation of the laser powder-bed fusion process, Addit. Manuf. 16 (2017) 73–80, https://doi.org/10.1016/j.addma.2017.05.001.

[37] E.R. Denlinger, J. Irwin, P. Michaleris, Thermomechanical modeling of additive manufacturing large parts, Trans. ASME J. Manuf. Sci. Eng. 136 (6) (2014), 061007.

[38] M. Gouge, P. Michaleris, Thermo-Mechanical Modeling of Additive Manufacturing, Elsevier, Cambridge, MA, 2018.

[39] D. Pal, N. Patil, K. Zeng, B. Stucker, An integrated approach to additive manufacturing simulations using physics based, coupled multiscale process

modeling, J. Manuf. Sci. Eng. 136 (6) (2014) 061022–061022-061016, https://doi.org/10.1115/1.4028580.
[40] J.A. Goldak, M. Akhlaghi, Computational Welding Mechanics, Springer, New York, 2006.
[41] M. Markl, C. Körner, Multiscale modeling of powder bed–based additive manufacturing, Annu. Rev. Mater. Res. 46 (1) (2016) 93–123, https://doi.org/10.1146/annurev-matsci-070115-032158.
[42] D. Bourell, J.P. Kruth, M. Leu, G. Levy, D. Rosen, A.M. Beese, A. Clare, Materials for additive manufacturing, CIRP Ann. 66 (2) (2017) 659–681, https://doi.org/10.1016/j.cirp.2017.05.009.
[43] S.A. Khairallah, A.T. Anderson, A. Rubenchik, W.E. King, Laser powder-bed fusion additive manufacturing: physics of complex melt flow and formation mechanisms of pores, spatter, and denudation zones, Acta Mater. 108 (2016) 36–45.
[44] B.W. Martin, T.K. Ales, M.R. Rolchigo, P.C. Collins, 17 - Developing and applying ICME + modeling tools to predict performance of additively manufactured aerospace parts, in: F. Froes, R. Boyer (Eds.), Additive Manufacturing for the Aerospace Industry, Elsevier, 2019, pp. 375–400.
[45] T. Gatsos, K.A. Elsayed, Y. Zhai, D.A. Lados, Review on computational modeling of process–microstructure–property relationships in metal additive manufacturing, JOM 72 (1) (2020) 403–419, https://doi.org/10.1007/s11837-019-03913-x.
[46] A. Polonsky, Three-Dimensional Characterization of Additively Manufactured Metals (Ph.D. Dissertation), UC Santa Barbara, 2020.
[47] C.R. Fisher, C.E. Vail, Computational simulation of an additively manufactured marine component, J. Mater. Eng. Perform. 28 (2018) 627–632, https://doi.org/10.1007/s11665-018-3603-4.
[48] E. Kundakcioglu, I. Lazoglu, S. Rawal, Transient thermal modeling of laser-based additive manufacturing for 3D freeform structures, Int. J. Adv. Manuf. Technol. 85 (1) (2016) 493–501, https://doi.org/10.1007/s00170-015-7932-2.
[49] H. Peng, M. Ghasri-Khouzani, S. Gong, R. Attardo, P. Ostiguy, R.B. Rogge, B. A. Gatrell, J. Budzinski, C. Tomonto, J. Neidig, M.R. Shankar, R. Billo, D.B. Go, D. Hoelzle, Fast prediction of thermal distortion in metal powder bed fusion additive manufacturing: part 2, a quasi-static thermo-mechanical model, Addit. Manuf. 22 (2018) 869–882, https://doi.org/10.1016/j.addma.2018.05.001.
[50] F. Dugast, P. Apostolou, A. Fernandez, W. Dong, Q. Chen, S. Strayer, R. Wicker, A. C. To, Part-scale thermal process modeling for laser powder bed fusion with matrix-free method and GPU computing, Addit. Manuf. (2020), 101732, https://doi.org/10.1016/j.addma.2020.101732.
[51] A.J. Dunbar, E.R. Denlinger, J. Heigel, P. Michaleris, P. Guerrier, R. Martukanitz, T. W. Simpson, Development of experimental method for in situ distortion and temperature measurements during the laser powder bed fusion additive manufacturing process, Addit. Manuf. 12 (2016) 25–30, https://doi.org/10.1016/j.addma.2016.04.007.
[52] N. Wood, H. Mendoza, P. Boulware, D.J. Hoelzle, Interrogation of mid-build internal temperature distributions within parts being manufactured via the powder bed fusion process, in: Proceedings of the 2019 Annual International Solid Freeform Fabrication Symposium, (2019).
[53] R.J. Williams, C.M. Davies, P.A. Hooper, A pragmatic part scale model for residual stress and distortion prediction in powder bed fusion, Addit. Manuf. 22 (2018) 416–425, https://doi.org/10.1016/j.addma.2018.05.038.
[54] P. Promoppatum, S.-C. Yao, P.C. Pistorius, A.D. Rollett, P.J. Coutts, F. Lia, R. Martukanitz, Numerical modeling and experimental validation of thermal history and microstructure for additive manufacturing of an Inconel 718 product, Prog. Addit. Manuf. 3 (1) (2018) 15–32, https://doi.org/10.1007/s40964-018-0039-1.
[55] S. Moylan, E. Whitenton, B. Lane, J. Slotwinski, Infrared thermography for laser-based powder bed fusion additive manufacturing processes, AIP Conf. Proc. Am. Inst. Phys. (2014) 1191–1196.
[56] B. Lane, L. Jacquemetton, M. Piltch, D. Beckett, Thermal calibration of commercial melt pool monitoring sensors on a laser powder bed fusion system, NIST Adv. Manuf. Ser. (2020) 100–135.
[57] P.A. Hooper, Melt pool temperature and cooling rates in laser powder bed fusion, Addit. Manuf. 22 (2018) 548–559, https://doi.org/10.1016/j.addma.2018.05.032.
[58] G. Mohr, N. Scheuschner, K. Hilgenberg, In situ heat accumulation by geometrical features obstructing heat flux and by reduced inter layer times in laser powder bed fusion of AISI 316L stainless steel, Procedia CIRP 94 (2020) 155–160, https://doi.org/10.1016/j.procir.2020.09.030.
[59] B. Xiao, E.R. Hancock, R.C. Wilson, Graph characteristics from the heat kernel trace, Pattern Recognit. 42 (11) (2009) 2589–2606.
[60] F. Zhang, E.R. Hancock, Graph spectral image smoothing using the heat kernel, Pattern Recognit. 41 (11) (2008) 3328–3342, https://doi.org/10.1016/j.patcog.2008.05.007.
[61] Y.A. Çengel, A.J. Ghajar, Heat and Mass Transfer: Fundamentals & Applications., McGraw Hill, New York, 2011.
[62] J.C. Heigel, P. Michaleris, E.W. Reutzel, Thermo-mechanical model development and validation of directed energy deposition additive manufacturing of Ti–6Al–4V, Addit. Manuf. 5 (2015) 9–19, https://doi.org/10.1016/j.addma.2014.10.003.
[63] A. Gaikwad, R. Yavari, M. Montazeri, K. Cole, L. Bian, P. Rao, Toward the digital twin of additive manufacturing: Integrating thermal simulations, sensing, and analytics to detect process faults, IISE Trans. 52 (11) (2020) 1204–1217, https://doi.org/10.1080/24725854.2019.1701753.